

1 **Quantifying Isentropic Mixing in a Modified Lagrangian Coordinate:**

2 **Applications to Rossby Wave Breaking**

3 Chengji Liu\* and Elizabeth A. Barnes

4 *Department of Atmospheric Sciences, Colorado State University, Fort Collins, Colorado*

5 *\*Corresponding author address: Department of Atmospheric Sciences, Colorado State University,*

6 *Fort Collins, Colorado.*

7 *E-mail: [cjliu@atmos.colostate.edu](mailto:cjliu@atmos.colostate.edu)*

## ABSTRACT

8 Isentropic mixing is an important process for the distribution of chemical  
9 constituents in the mid-to-high latitudes. A new framework is introduced to  
10 quantify both symmetric and asymmetric isentropic mixing in a modified La-  
11 grangian coordinate. The framework is applied to quantify the mixing asso-  
12 ciated with the two types of Rossby wave breaking (i.e. cyclonic and anticy-  
13 clonic) in two sets of idealized numerical simulations – eddy lifecycle sim-  
14 ulations and a long climate simulation. In both sets of simulations, cyclonic  
15 wave breaking (CWB) exhibits either comparable or stronger mixing than an-  
16 ticyclonic wave breaking (AWB). Since CWB occurs less frequently while  
17 AWB occurs more frequently when the jet shifts poleward, this difference in  
18 mixing strength between the two types of Rossby wave breaking translates  
19 into a change in total isentropic mixing when the jet shifts. Specifically, it  
20 is found in the climate simulation that as the jet shifts poleward, symmetric  
21 mixing is weakened in the underworld and both symmetric and asymmetric  
22 mixing across the tropopause is weakened in the mid-to-high latitudes. The  
23 dynamical relationship above is relevant not only for internal climate variabil-  
24 ity such as the El-Niño Southern Oscillation (ENSO) and the annular modes,  
25 but also, for future climate change that may drive changes in the jet position.

## 1. Introduction

Atmospheric transport and mixing play a fundamental role in the global distribution of chemical pollutants and moisture. In the extratropics, transport and mixing by eddies are known to mainly operate along isentropic surfaces, i.e. constant potential temperature ( $\theta$ ) surfaces. Within the troposphere, warm conveyor belts embedded in extratropical cyclones transport warm moist air poleward and upward along sloped isentropes (e.g. Thorncroft et al., 1993; Madonna et al., 2014). These transport events are responsible for poleward moisture transport (e.g. Eckhardt et al., 2004) and pollutant transport into the Arctic (e.g. Raatz and Shaw, 1984; Barrie, 1986). In the upper troposphere, vigorous exchange between stratospheric and tropospheric constituents happens along isentropes across a folding tropopause (e.g. Shapiro, 1980). Such exchange is an important source of ozone in the troposphere (e.g. Lelieveld and Dentener, 2000) where it is considered a pollutant and is detrimental to human health (e.g. Lippmann, 1989). This exchange also injects anthropogenic trace species such as chlorofluorocarbon (CFC) into the stratosphere (Holton et al., 1995).

Due to the dominance of isentropic transport and mixing in the extratropics,  $\theta$  is often used as the vertical coordinate in quantifying these processes. Under the adiabatic approximation,  $\theta$  can be considered a material surface and hence a Lagrangian coordinate. A Lagrangian coordinate is a more natural choice than a Eulerian one for transport and mixing since it avoids the need for Stokes correction for artifacts arising from the Eulerian-mean (McIntyre, 1980). With  $\theta$  being the vertical coordinate, reversible vertical oscillations are absent and any vertical flux is associated with diabatic heating. Along these same lines, it is natural to also choose a conserved variable as the meridional coordinate so that any meridional flux in such a coordinate is only associated with non-conservative processes, such as horizontal diffusion. Examples include using potential vor-

49 ticity (PV) or the concentration of a passive tracer as the meridional coordinate (e.g. Butchart and  
50 Remsberg, 1986). By integrating quantities between contours of a conserved quantity, a general  
51 description of the irreversible mixing is possible without expensive trajectory calculations.

52 In such a Lagrangian coordinate, diffusive processes can alter the budget of a quantity within a  
53 coordinate contour in two ways. The first way is by changing the mass enclosed by a contour. As  
54 we will show later, this is done by net mass flux across the contour through what we call asymmet-  
55 ric mixing. The other way is by changing the concentration of the quantity within a contour. This  
56 is done by down-gradient mixing across the contour which we call symmetric mixing. However,  
57 we are not aware of any study that has quantified both processes in a modified Lagrangian coor-  
58 dinate. Nakamura (1995) proposed the modified Lagrangian mean (MLM) continuity equation to  
59 quantify net mass flux due to non-conservative processes, which specifically isolates asymmetric  
60 mixing in the horizontal direction. More recent studies that use this framework (e.g. Nakamura,  
61 2004, 2007; ?) are also focused solely on asymmetric mixing. On the other hand, Nakamura  
62 (1996) studied the distribution of a passive tracer in non-divergent barotropic flow and used the  
63 mass (i.e. area) enclosed by the tracer as the meridional coordinate. In such a coordinate, the net  
64 mass flux is zero by construction and symmetric mixing alone determines the distribution of the  
65 passive tracer. Under these conditions, he derived the MLM tracer equation in a diffusive form and  
66 proposed the “effective diffusivity”. Other studies that have used the effective diffusivity (or its  
67 generalized form) also focus on symmetric mixing (e.g. Haynes and Shuckburgh, 2000a,b; Chen  
68 and Plumb, 2014; ?; Abalos et al., 2016). In this study, we propose a new framework to quan-  
69 tify both symmetric and asymmetric mixing in a modified Lagrangian coordinate, and apply it to  
70 synoptic eddy lifecycle simulations and a climate simulation.

71 As there are many ways to quantify isentropic mixing, there are many physical processes that  
72 drive them. Among them, Rossby wave breaking (RWB) is an important one both within the

73 troposphere and across the tropopause. Near the tropopause, RWB has been shown by numerous  
74 studies to be associated with the exchange of mass or chemical tracers between the stratosphere and  
75 the troposphere (e.g. Appenzeller and Davies, 1992; Trepte et al., 1993; Chen, 1995; Appenzeller  
76 et al., 1996; Jing et al., 2004). Especially strong exchange occurs in the presence of a double  
77 tropopause (e.g. Randel et al., 2007; Pan et al., 2009) which is a feature related to RWB (e.g.  
78 Wang and Polvani, 2011). In the troposphere, we will show that RWB is also closely linked to  
79 isentropic mixing.

80 RWB can be classified into two distinct types – anticyclonic wave breaking (AWB) and cyclonic  
81 wave breaking (CWB), and the frequency of each is strongly coupled to the midlatitude jet stream.  
82 Climatologically, AWB occurs most frequently on the equatorward flank of the jet where the hor-  
83 izontal wind shear is anticyclonic, while CWB occurs most frequently on the poleward flank of  
84 the jet. As the jet shifts poleward, the total frequency of AWB increases whereas that of CWB  
85 decreases (e.g. Strong and Magnusdottir, 2008; ?; Rivière, 2011; Barnes and Hartmann, 2012).  
86 This RWB-jet position relationship is especially important because the jet stream position is very  
87 responsive to both internal climate variability such as the El-Niño Southern Oscillation (ENSO)  
88 (e.g. Rasmusson and Wallace, 1983; Chen and van den Dool, 1999; Ren et al., 2008), and exter-  
89 nal climate forcings such as increasing greenhouse gas concentrations and ozone depletion (e.g.  
90 Thompson and Solomon, 2002; Butler et al., 2010; Barnes and Polvani, 2013). It is through such  
91 coupling that RWB is linked to climate variability on different time scales, and thus, can drive the  
92 variability of global transport and mixing of various chemical tracers.

93 Quantifying the isentropic mixing by RWB is thus key to understanding the variability of the  
94 climate-scale distribution of various chemical tracers. Polvani and Esler (2007) (hereafter PE07)  
95 quantified the combined symmetric and asymmetric mixing associated with the two types of RWB  
96 in idealized eddy lifecycle simulations. They found that CWB exhibits stronger mixing from the

97 stratosphere to the troposphere compared to AWB. Considering the coupling of the jet stream  
98 position and AWB vs. CWB frequency, such a difference has significant implications since it  
99 may translate into a change in total mixing when the jet stream shifts. In this work, we explore  
100 these implications by asking two questions: (1) Is there a robust difference in asymmetric and  
101 symmetric mixing efficiency between AWB and CWB? (2) How does this difference, if it exists,  
102 translate into a dependence of total mixing on jet variability?

103 The paper is organized as follows. A description of the numerical simulations is given in section  
104 2. In section 3, we introduce a new framework to quantify both symmetric and asymmetric mixing  
105 in a modified Lagrangian coordinate. Section 4 revisits the idealized simulations of PE07 and  
106 demonstrates how our new framework can provide additional insight. Section 5 explores both  
107 types of mixing linked to RWB in a climate simulation, and tests the robustness of the difference  
108 between AWB and CWB. Section 6 shows how such difference can impact total mixing as the the  
109 jet-stream shifts. Conclusions are given in section 7.

## 110 **2. Model setups**

111 All simulations in this study are performed by integrating a primitive equation model with no  
112 topography. The specific model used is the Geophysical Fluid Dynamics Laboratory (GFDL)  
113 spectral dry dynamical core with a horizontal resolution of T42, and an integrating time step  
114 of 1200 seconds. The model uses  $\nabla^8$  horizontal hyperdiffusion for dynamical variables such as  
115 temperature, vorticity and divergence. There is no explicit vertical diffusion for any variable in  
116 this model.

117 With the same model setup described above, we carry out two different sets of simulations. The  
118 first set of simulations are idealized eddy lifecycle simulations with initialized passive tracers that  
119 follow PE07 (to be discussed in detail). In this simulation, we aim to validate our new framework

120 for quantifying isentropic mixing by applying it to stratosphere-troposphere-exchange (STE) in  
 121 the identical setting used by PE07, and to gain additional insight. The second simulation is an  
 122 idealized climate run based on Held and Suarez (1994). In this simulation we investigate the  
 123 difference in the strength of AWB and CWB related mixing in an idealized climate setting, and  
 124 use the results to explain the dependence of isentropic mixing on jet variability. The detailed  
 125 configuration for these two simulations is described in the next two subsections.

126 *a. Idealized eddy lifecycle simulation*

127 Following PE07, we reproduce the two idealized eddy lifecycles (LC1 and LC2) first introduced  
 128 by Thorncroft et al. (1993). The model is configured with 30 unevenly spaced vertical layers and  
 129 no diabatic heating during the 20-day run. In both the LC1 and LC2 simulations, only the initial  
 130 conditions are prescribed. For LC1, a baroclinically unstable jet is prescribed on day 1 and the  
 131 eddies grow and break anticyclonically at the late stages of its lifecycle, which corresponds to  
 132 AWB in the real atmosphere. The initial zonal wind is given by:

$$u_1(\phi, z) = U_0 F(\phi) [(z/z_T) e^{-[(z/z_T)^2 - 1]/2}] \quad (1a)$$

$$F(\phi) = \begin{cases} [\sin(\pi(\sin\phi)^2)]^3, & \text{for } \phi > 0 \\ 0, & \text{for } \phi < 0. \end{cases} \quad (1b)$$

134 where  $z \equiv H \log(p_0/p)$  is the log-pressure height. For LC2, the initial zonal wind is obtained by  
 135 adding a bottom-heavy cyclonic shear  $u_s$  to the initial wind profile for LC1,

$$u_2(\phi, z) = u_1(\phi, z) + u_s(\phi, z) \quad (2a)$$

$$u_s(\phi, z) = -U_s e^{-z/z_s} [\sin(2\phi)]^2 \left[ \frac{\phi - \phi_s}{\Delta_s} \right] e^{-[\frac{\phi - \phi_s}{\Delta_s}]^2} \quad (2b)$$

137 In the LC2 simulation the eddies grow and break cyclonically at the late stages of the lifecycle  
 138 which corresponds to CWB. The constants appearing in (1) and (2) are the same as those in PE07.  
 139 For both lifecycles, the initial conditions for temperature and surface pressure are set to be in  
 140 thermal wind balance with the zonal wind profiles prescribed in (1) and (2). See appendix A of  
 141 PE07 for the additional details on calculating these balanced initial conditions. In addition to the  
 142 balanced temperature profile, a wavenumber-6 perturbation centered at 45°N is added to the initial  
 143 temperature field to give rise to the growing eddies.

144 For both the LC1 and LC2 simulations, the tracer setup is similar to PE07 in that we initialize  
 145 two passive isentropic tracers: a stratospheric tracer ( $S$ ) and a tropospheric tracer ( $T$ ) on isentropes  
 146 ranging from 290K to 380K. The initial tropopause is defined in PE07 as a nearly vertical boundary  
 147 that partitions isentropes into a poleward half (stratosphere) and an equatorward half (troposphere)  
 148 (see Fig. 5 in PE07). The initial concentrations of the two tracers are set such that poleward of the  
 149 initial tropopause  $S = 1$  and  $T = 0$ , while equatorward of it  $T = 1$  and  $S = 0$ . Since the simulations  
 150 are adiabatic,  $S + T = 1$  on isentropes from 290K to 380K at all times by construction. During  
 151 the simulations, the tropopause is defined by an evolving boundary between the two tracers as the  
 152 contour of  $S = T = 0.5$ . Both  $S$  and  $T$  are spectral tracers and a  $\nabla^8$  hyperdiffusion is applied at  
 153 each time step. We refer readers to PE07 for additional details.

#### 154 *b. Idealized climate simulation*

155 We perform a climate simulation forced by the idealized diabatic heating scheme proposed by  
 156 Held and Suarez (1994). Specifically, we set the diabatic heating as a relaxation to a prescribed  
 157 zonally-symmetric equilibrium temperature profile:

$$T_{eq} = \max \left\{ 200K, \left[ \underbrace{315K}_{A} - \underbrace{(\Delta T)_y \sin^2 \phi}_{B} - \underbrace{(\Delta \theta)_z \log \left( \frac{p}{p_0} \right) \cos^2 \phi}_{C} - \underbrace{\epsilon \sin \phi}_{D} \right] \underbrace{\left( \frac{p}{p_0} \right)^{\kappa}}_{D} \right\} \quad (3)$$

158 For this relaxation scheme, the individual terms in (3) are equivalent to constant heating or cooling  
159 terms. Idealized as it is, (3) includes the most essential elements of climate forcing – heating in low  
160 latitudes and cooling in high latitudes, as represented by term A. Term B is a modification for the  
161 tropics, as manifested by the  $\cos^2\phi$  factor. Without term B, but with the inclusion of factor D, (3)  
162 would yield an atmosphere that was stratified dry adiabatically. Term B thus can be thought of as a  
163 representation of stabilization by moist convection in the tropics which is not represented explicitly  
164 in this model setup. Term C adds a hemispheric asymmetry to the equilibrium temperature that  
165 accounts for seasonality in radiative forcing. In this study we set  $\varepsilon = 10$  which represents winter  
166 conditions in the Northern Hemisphere. We focus on winter because the eddy activity is strongest  
167 in winter when the baroclinicity is largest. In addition, the low frequency variability that modulates  
168 eddy activity (e.g. the annular mode) is also strongest in the winter.

169 While the equilibrium temperature profile given in (3) leads to a midlatitude circulation that is  
170 generally representative of that is observed, there are still noticeable differences, especially in the  
171 tropics. For example, the Hadley cell in this dry general circulation model (GCM) is substantially  
172 weaker than in observations. However, the main purpose of this simulation is not to reproduce the  
173 observed circulation exactly (there is no topography, for example), but to serve as a stepping stone  
174 between the unforced eddy lifecycle simulation and reality by removing the complexities of full  
175 GCMs that are not essential for isentropic mixing.

176 To study the isentropic mixing along isentropes, we initialize a spectral tracer that serves as  
177 our Lagrangian coordinate. The tracer can be thought of having a source in the boundary layer  
178 from  $60^\circ\text{S}$  to  $60^\circ\text{N}$  and a sink that includes the entire atmospheric column at the poles so that an  
179 equator-to-pole gradient in tracer concentration is maintained along isentropic surfaces. As will  
180 be explained in the next section, this monotonic meridional gradient of the tracer is required for  
181 our tracer coordinate system. The tracer concentration is set to 0 anywhere poleward of  $85^\circ\text{N}$  or

182 85°S, and

$$\frac{1}{4.5} [3.7 - P_2(\sin\phi) - P_4(\sin\phi)] \quad (4)$$

183 in the boundary layer.  $P_2$  and  $P_4$  are the second and fourth order Legendre polynomials respec-  
184 tively. (4) is qualitatively similar to a tracer concentration of 1 from 60°S to 60°N and 0 elsewhere  
185 in the boundary layer, but with a gradual transition from 1 to 0 on the edges, which prevents spu-  
186 rious tracer concentration during integration due to Gibbs effect. The tracer is otherwise passive  
187 throughout the rest of the atmosphere. As in the lifecycle simulations, a  $\nabla^8$  hyperdiffusion is used  
188 for the spectral tracer.

189 With the setup described above, the model is run with 20 evenly spaced sigma levels for 25  
190 years. We use the last 22 years for analysis which allows for a spin-up period of about 1000 days.  
191 All of the variables are output every 6 hours.

### 192 **3. Quantification of isentropic symmetric and asymmetric mixing**

#### 193 *a. MLM framework and the tracer equation*

194 Viewed in an Eulerian framework, the distribution of a passive tracer can be accounted for by two  
195 processes: advective fluxes and diffusive fluxes. The idea of a modified Lagrangian coordinate is  
196 to reformulate the Eulerian tracer equation in a flow-following two-dimensional coordinate so that  
197 reversible advective fluxes are absent. Specifically, we can choose potential temperature ( $\theta$ ) as the  
198 vertical coordinate, and the concentration of a passive tracer ( $q$ ) as the meridional coordinate. As  
199 shown by Nakamura (1995), under such a coordinate transformation, the mass continuity equation  
200 becomes:

$$\frac{\partial \mathcal{M}(1)}{\partial t} = -\frac{\partial \mathcal{M}(q)}{\partial q} - \frac{\partial \mathcal{M}(\dot{\theta})}{\partial \theta} \quad (5)$$

201 where  $\dot{q}$  and  $\dot{\theta}$  are the material derivatives of  $q$  and  $\theta$ , and

$$\mathcal{M}(\cdot) \equiv \iint_{q^* \leq q} (\cdot) \sigma dA = \int_{q^* \leq q} dq^* \oint_{q^*} \frac{(\cdot) \sigma}{|\nabla_{\theta} q^*|} dl \quad (6a)$$

202

$$\frac{\partial \mathcal{M}(\cdot)}{\partial q} = \oint_q \frac{(\cdot) \sigma}{|\nabla_{\theta} q^*|} dl \quad (6b)$$

203 in which  $\sigma \equiv -g^{-1} \frac{\partial p}{\partial \theta}$  is the pseudo-density in isentropic coordinates. Note that in the climate  
 204 simulation  $q$  decreases with latitude as determined by the sources and sinks of our passive tracer.  
 205 On the *lhs* of (5) is the mass tendency within a contour of  $q$ . The first term on the *rhs* of (5)  
 206 accounts for horizontal transport of mass across a contour of  $q$ , while the second term represents  
 207 the differential vertical transport of mass across isentropic surfaces. These transport terms are  
 208 proportional to the magnitudes of  $\dot{q}$  and  $\dot{\theta}$  which represent tendencies due to non-conservative  
 209 processes such as diffusion and diabatic heating. These non-conservative processes correspond  
 210 to irreversible transport and mixing of an air mass. Conservative processes such as reversible  
 211 advection are invisible to (5).

212 We can now write the MLM equation for the mass budget of a tracer  $\chi$  within a contour of  $q$ :

$$\frac{\partial \mathcal{M}(\chi)}{\partial t} = -\frac{\partial \mathcal{M}(\dot{q}\chi)}{\partial q} - \frac{\partial \mathcal{M}(\dot{\theta}\chi)}{\partial \theta} + \mathcal{M}(\dot{\chi}) \quad (7)$$

213 and we refer the reader to Appendix A for the derivation. The first three terms are very similar  
 214 to the three terms in (5). This connection is clearer if one thinks of  $\chi$  as a ubiquitous tracer with  
 215 a concentration of 100% ( $\chi=1$ ) everywhere. In this special case, plugging  $\chi=1$  into (7) reduces  
 216 the tracer equation to the mass continuity equation (5), where  $\mathcal{M}(\dot{\chi})$  vanishes since  $\dot{\chi} = 0$ . For  
 217 a general tracer  $\chi$ , the first two terms on the *rhs* of (7) are mass flux weighted by the tracer  
 218 concentration and represent the effective advection of  $\chi$ . As will be shown in the next subsection,  
 219 this ‘‘advection’’ is due to *asymmetric mixing* on the two sides of the coordinate contour. The

220 physical meaning of the third term,  $\mathcal{M}(\dot{\chi})$ , is two-fold since  $\dot{\chi}$  can be partitioned into two parts:

$$\dot{\chi} = \dot{\chi}_{diff} + \dot{\chi}_{prod}$$

221 The first term is the tendency due to diffusion ( $\dot{\chi}_{diff}$ ), and the second term is the tendency due to  
 222 tracer production and loss ( $\dot{\chi}_{prod}$ ), for example, due to chemical reaction or phase change. Due to  
 223 the linearity of operator  $\mathcal{M}(\cdot)$ , we can partition  $\mathcal{M}(\dot{\chi})$  accordingly:

$$\mathcal{M}(\dot{\chi}) = \mathcal{M}(\dot{\chi}_{diff}) + \mathcal{M}(\dot{\chi}_{prod}) \quad (8)$$

224 The physical meaning of  $\mathcal{M}(\dot{\chi}_{prod})$  is thus the change in the tracer mass of  $\chi$  within a tracer  
 225 contour of  $q$  due to the area-integrated production within the  $q$  contour. The reason the produc-  
 226 tion does not show up in (5) is simply that mass cannot be generated or destroyed. In this study,  
 227 we focus on the dynamic aspect of equation (7) and thus will only use a passive tracer so that  
 228  $\mathcal{M}(\dot{\chi}_{prod}) = 0$  at all times. The physical meaning of  $\mathcal{M}(\dot{\chi}_{diff})$  is less straightforward and repre-  
 229 sents the *symmetric mixing* of tracer  $\chi$  into a  $q$  contour by swapping mass across the contour. That  
 230 is, although the air is refreshed on both sides, the amount of mass on either side remains constant,  
 231 and thus, total mass flux is zero which is why it does not appear in the mass continuity equation  
 232 (5). We will further justify the interpretation of this term as symmetric mixing in the following  
 233 subsection.

### 234 *b. Isentropic asymmetric and symmetric mixing*

235 The interpretation of the first and third terms on the *rhs* of equation (7) is most clear if we let  
 236  $\chi=q$ , namely, we use the tracer of interest as our meridional coordinate. In this case, we have an  
 237 equation for the mass budget of  $q$  within a contour of  $q$ :

$$\frac{\partial \mathcal{M}(q)}{\partial t} = -\frac{\partial \mathcal{M}(\dot{q})}{\partial q} q - \frac{\partial \mathcal{M}(\dot{\theta} q)}{\partial \theta} + \mathcal{M}(\dot{q}) \quad (9)$$

238 where we have used the fact that:

$$\frac{\partial \mathcal{M}(\dot{q}q)}{\partial q} = \oint_q \frac{\dot{q}^* q^*}{|\nabla_{\theta} q^*|} \sigma dl = \oint_q \frac{\dot{q}^*}{|\nabla_{\theta} q^*|} \sigma dl \cdot q = \frac{\partial \mathcal{M}(\dot{q})}{\partial q} q$$

239 The third term on the *rhs* of (9) is termed symmetric mixing in this study. It appears as an area  
240 integral in (9) but can be thought of as a line integral if  $\dot{q}$  takes a diffusive form such as:

$$\dot{q} = \kappa \nabla_{\theta}^2 q = \kappa \nabla_{\theta} \cdot \nabla_{\theta} q \quad (10)$$

241 Plugging (10) into the term  $\mathcal{M}(\dot{q})$  and applying the divergence theorem leads to

$$\mathcal{M}(\dot{q}) = \kappa \oint_q |\nabla_{\theta} q^*| \sigma dl \quad (11)$$

242 The magnitude of  $\mathcal{M}(\dot{q})$  is thus proportional to the gradient of the tracer  $q$  across the contour.

243 In the case of non-divergent barotropic flow,  $\sigma$  is a constant ( $\sigma = \sigma_0$ ) and we can rewrite  $\mathcal{M}(\dot{q})$   
244 in a diffusive form through application of (6b):

$$\mathcal{M}(\dot{q}) = \sigma_0 \kappa_{eff} \frac{\partial q}{\partial A} \quad (12)$$

245 where  $A(q, \theta, t)$  is the area enclosed by a contour  $q$ , and

$$\kappa_{eff} = \kappa \frac{\partial}{\partial A} \iint |\nabla_{\theta} q|^2 dA / \left( \frac{\partial q}{\partial A} \right)^2 \quad (13)$$

246 is identical to the effective diffusivity proposed by Nakamura (1996). (See Appendix B for the  
247 derivation.) The fact that we can write  $\mathcal{M}(\dot{q})$  as an effective diffusivity times the tracer gradi-  
248 ent further justifies our interpretation of this term as representing symmetric mixing. Note that  
249 the effective diffusivity  $\kappa_{eff}$  in the form of (13) is positive definite so the sign of the mixing is  
250 determined only by the tracer gradient in this instance.

251 The first term on the *rhs* of (9) is the product of the meridional net mass flux,  $-\partial \mathcal{M}(\dot{q})/\partial q$ , and  
252 the tracer concentration  $q$ . The interpretation of the mass flux term is two-fold. On the one hand, it  
253 balances the vertical diabatic mass flux,  $-\partial \mathcal{M}(\dot{\theta})/\partial \theta$ , in the climatological mean and thus is part

254 of the diabatic circulation. Leibensperger and Plumb (2014) use the diabatic mass flux to define a  
255 meridional advection term in their MLM tracer equation, which takes an advection-diffusion form.  
256 In light of this, the  $-q\partial\mathcal{M}(\dot{q})/\partial q$  term has the effect of “advection” in our Lagrangian coordinate.  
257 On the other hand, the meridional mass flux arises from asymmetric isentropic mixing. This is  
258 mathematically evident since the mass flux is the meridional gradient of the symmetric mixing  
259 term  $\mathcal{M}(\dot{q})$  as shown in (9). Physically, mixing acts to reduce the gradient of a passive tracer and  
260 pushes the tracer contours farther away from each other. For a particular tracer contour, if the  
261 strength of symmetric mixing is not equal on its two sides, the tracer contour will be pushed away  
262 from the region of stronger mixing, accompanied by a change in its latitude. Alternatively one can  
263 visualize this as an increase in air mass on the side of the tracer contour with stronger mixing.

264 Based on the discussion above, we refer to the first term on the *rhs* of (9) as *asymmetric mixing*,  
265 and the third term as *symmetric mixing*. As has been discussed and will be shown, the two have  
266 very different behaviors. The asymmetric mixing is directional and its direction is dictated by the  
267 mass flux. The symmetric mixing is diffusive and its direction is down-gradient.

### 268 *c. Calculation of asymmetric and symmetric mixing*

269 To calculate the asymmetric and symmetric mixing terms in (9), we need to first determine  
270 the tracer contours to use as coordinates. In the idealized lifecycle simulations, the only contour  
271 used is the 0.5 contour for both  $S$  and  $T$  tracers which defines the tropopause. For the climate  
272 simulation, we pick 32 contours of  $q$  for each isentropic level in the Northern Hemisphere. What  
273 follows describes how these 32 contours are chosen. We determine these 32 values of  $q$  by the  
274 one-to-one relationship between  $q$  and equivalent latitude  $\phi_e$  (Butchart and Remsberg, 1986) on

275 each isentrope and at each time step:

$$\phi_e(q) = \arcsin \left[ 1 - \frac{A(q)}{2\pi a^2} \right] \quad (14)$$

276 Specifically, we pick 32 values of  $\phi_e$  and then obtain the 32 values of  $q(\phi_e)$  by reversing the rela-  
 277 tionship of (14) at each time step. Finally, we temporally average  $q(\phi_e)$  over a year of simulation  
 278 and use these averaged  $q(\phi_e)$  as the meridional coordinate. All of the MLM mixing results, how-  
 279 ever, are displayed with the corresponding equivalent latitude ( $\phi_e$ ) along the x-axis.

280 The terms in (9) are calculated as area integrals of combinations of  $\sigma$  and  $\dot{q}$ .  $\dot{q}$  is calculated as  
 281 the 4th order hyperdiffusion in the model, and we output  $\dot{q}$  at 6-hourly intervals and interpolate  
 282 it and  $\sigma$  on isentropic surfaces following the interpolation scheme by Edouard et al. (1997). The  
 283 integration area for the numerator in the asymmetric mixing term,  $\partial \mathcal{M}(\dot{q})$ , is shown in Fig. ??a as  
 284 a thin green band. The denominator  $\partial q$  is calculated as the difference  $q_1 - q_2$  of the two contours  
 285 that bound the green area. The integration area for the symmetric mixing term,  $\mathcal{M}(\dot{q})$ , is illustrated  
 286 in Fig. ??b. For the climate simulation, we are especially interested in mixing driven by eddies.  
 287 To serve this purpose, we partition the integration for  $\mathcal{M}(\dot{q})$  into two parts following the idea of  
 288 Chen and Plumb (2014):

$$\mathcal{M}(\dot{q}) = \overline{\mathcal{M}}(\dot{q}) + \Delta \mathcal{M}(\dot{q}) \quad (15)$$

289 The first term is  $\overline{\mathcal{M}}(\dot{q})$  which represents the integration poleward of an equivalent latitude circle  
 290 ( $\phi_e$ ). The integration area for this term is indicated by the black dashed circle in Figs. ??b-d. This  
 291 term is driven only by diffusion. The second term is  $\Delta \mathcal{M}(\dot{q})$  which is driven by zonal asymmetries  
 292 in the flow (i.e. eddies). The integration area of this term is indicated by the shading in Fig  
 293 ??d where the red area is weighted by 1 and the blue area is weighted by  $-1$ .  $\Delta \mathcal{M}(\dot{q})$  captures  
 294 symmetric mixing by eddies (from now on referred to as eddy mixing) and is the component we  
 295 focus on here.

296 Although in this study we focus on idealized settings where only passive tracers are used, (9)  
297 can be applied to more realistic and sophisticated tracers in GCMs if diffusion is calculated ex-  
298 plicitly. In that case, using (9) along with (8) one can separate the contributions from asymmetric,  
299 symmetric mixing and chemical production and loss to the distribution of a species.

300 *d. Linking asymmetric and symmetric mixing to Rossby wave breaking*

301 In this study, we separate mixing by the overturning direction of Rossby wave breaking – anti-  
302 cyclonic and cyclonic – due to the robust dynamical relationship between the two types of wave  
303 breaking and the jet streams (e.g. Barnes and Hartmann, 2012). Note that Nakamura (2004) sep-  
304 arates asymmetric mixing into a poleward and an equatorward component. Since cyclonic and  
305 anticyclonic wave breaking events are comprised of a combination of poleward and equatorward  
306 mixing, our approach is distinct from this earlier work. For our idealized lifecycle simulations,  
307 linking asymmetric and symmetric mixing to the two types of wave breaking is straightforward.  
308 As in PE07, we assume all of the mixing in the LC1 simulation is linked to AWB while all of  
309 the mixing in the LC2 is linked to CWB. However, for the climate simulation in which AWB and  
310 CWB coexist every day along with other non-breaking waves, we need a dedicated algorithm to  
311 separate the contribution from the two types of wave breaking from all of the other processes. To  
312 serve this purpose, we first need to detect the two types of RWB in the model output. Unlike some  
313 previous studies where contours of potential vorticity (PV) on isentropes are used to identify wave  
314 breaking events (e.g. Strong and Magnusdottir, 2008; Liu et al., 2014; Liu and Barnes, 2015), we  
315 base our algorithm on the tracer contours themselves. In fact, the contours of the tracer  $q$  in our  
316 climate simulation align well with PV contours on isentropic surfaces and thus our method is very  
317 similar to that of previous studies (not shown). The reason we favor  $q$  over PV for RWB detection

318 is that our quantification of the mixing is based on  $q$  contours already. Thus, using  $q$  to detect  
319 RWB is natural for linking mixing to RWB events in our framework.

320 Specifically, we detect RWB based on wave lobes illustrated in Fig ??c and ??d. If the left-  
321 most/rightmost point of one lobe is to the left/right of its base line (shown as black dashed seg-  
322 ments), then we identify the lobe as overturning. We require the extent of overturning be at least  
323  $5.5^\circ$  of longitude to exclude small scale disturbances that are not linked to large-scale RWB. Then,  
324 according to the direction of overturning, we partition the overturning lobes into AWB and CWB.  
325 For example, in Fig ??d the overturning lobe is identified as CWB and marked by dark blue shad-  
326 ing. The eddy mixing  $\Delta\mathcal{M}(\dot{q})$  associated with this CWB lobe is the integration over the dark blue  
327 area in Fig ??d. Similarly, the asymmetric mixing associated with the CWB lobe is the part of  
328 the integration that overlaps with the lobe, as illustrated by dark green region in Fig ??c. The fre-  
329 quency of occurrence of RWB is defined as the ratio of RWB area to the total wave area (e.g. dark  
330 blue versus all shading in Fig ??d). We compared the climatology of RWB frequency obtained  
331 by this method with that obtained by an algorithm using PV contours (Liu et al., 2014; Liu and  
332 Barnes, 2015). They agree well with each other (not shown), thus further supporting our use of  $q$   
333 for identifying RWB in this study.

334 A caveat should be raised about local RWB contribution to symmetric mixing. Since the diver-  
335 gence theorem does not hold for local integration, identities (11) and (12) do not hold for the RWB  
336 contribution. In other words, the local contribution to symmetric mixing is not guaranteed to be  
337 down-gradient although the total symmetric mixing is, provided that the diffusion takes the form  
338 of (10).

#### 4. Idealized lifecycle simulations

With the new framework to quantify asymmetric and symmetric mixing introduced in the last section, we aim to achieve two goals in this section: (1) validate our new framework for quantifying the two components of total mixing, and (2) gain additional insight into the stratosphere-troposphere-exchange (STE) in the idealized experiments explored by PE07.

Figure ?? shows snapshots of tracer  $S$  on the 335K isentrope in the two idealized lifecycles, as also shown by PE07. Orange indicates the stratosphere and blue indicates the troposphere. On day 8, the anticyclonic overturning in LC1 is depicted by the blue shading equatorward of the tropopause (denoted by the black dashed line), and the cyclonic overturning in LC2 is depicted by orange shading poleward of the tropopause (Fig. ??c and ??d respectively). It is evident in Fig. ??c and ??d that CWB in LC2 is much more active in stretching and overturning the tropopause compared to AWB in LC1. As a result, there is a larger interface between the  $S$  and  $T$  tracers for mixing to work on for CWB. Consistent with this picture, PE07 documented 50% stronger stratosphere-to-troposphere combined mixing in LC2 than in LC1.

Figure ?? shows the detailed quantification of STE in the two idealized lifecycles. Dashed blue lines in the upper row shows the troposphere-to-stratosphere combined mixing quantified using PE07's method. Specifically, we show the evolution of the mass of tracer  $T$  poleward of the tropopause (0.5 contour) in LC1 (left) and LC2 (right) simulations. This corresponds to the time integration of the  $\frac{\partial \mathcal{M}(q)}{\partial t}$  term in (9) poleward of  $q = 0.5$ , with  $q = T$ . Positive slope of the dashed blue lines indicate an increase of  $T$  in the stratosphere, or a poleward combined mixing of tracer  $T$  into the stratosphere. Similarly, dashed blue lines in the bottom row of Fig. ?? show the stratosphere-to-troposphere combined mixing by integrating the mass of  $S$  poleward of the 0.5 contour. Negative slopes of the blue lines indicate a decrease of  $S$  in the stratosphere, or an

362 equatorward combined mixing of tracer  $S$  into the troposphere. The dashed blue lines in Fig. ??  
363 agree qualitatively with PE07 – LC2 is comparable to LC1 in terms of troposphere-to-stratosphere  
364 combined mixing but has much stronger stratosphere-to-troposphere combined mixing compared  
365 to LC1.

366 So far we have only looked at the combined mixing in these lifecycle simulations. With our  
367 new framework, we can now quantify the asymmetric and symmetric components separately. The  
368 time integration of asymmetric mixing is depicted as green lines while that of symmetric mixing is  
369 depicted as red lines in Fig. ?. Since the simulations are adiabatic, the second term on the *rhs* of  
370 (9), which represents the vertical transport by diabatic processes, is zero. This means the sum of  
371 the asymmetric and symmetric mixing terms should equal the total tracer change, namely, the sum  
372 of the green and red lines should align with the dashed blue lines. We verify this by plotting the  
373 sum of the asymmetric and symmetric mixing as solid blue lines in Fig. ?, and they align well  
374 with the dashed blue lines, lending strong support to our new method for calculating isentropic  
375 mixing.

376 Taking a closer look at the evolution of the two components of mixing in Fig. ?, one finds a  
377 symmetry of them between upper and lower panels. First, the green lines (which indicate asym-  
378 metric mixing) are the same between the upper and lower panels. Since asymmetric mixing is the  
379 product of net mass flux and tracer concentration, and is evaluated at  $S = T = 0.5$ , both the net  
380 mass flux and the tracer concentration are the same for the two tracers. Secondly, the red lines  
381 (which indicate symmetric mixing) are the exact opposite for  $q = T$  and  $q = S$ . This is due to the  
382 fact that  $S = 1 - T$ , or in other words, the two tracers constitute the whole air mass. As a result,  
383  $S$  and  $T$  have gradients of the same magnitude but in opposite directions. Since the symmetric  
384 mixing is determined by the gradient of the tracer, opposite gradients give rise to opposite mix-  
385 ing. Another feature that stands out in Fig. ? is that the symmetric mixing (red lines) exhibits a

386 monotonic change with time. This is because symmetric mixing is usually down-gradient and the  
387 gradient of the tracer is fixed to be the same sign by construction throughout the entire simulation.  
388 Specifically, the down-gradient direction for tracer  $T$  is always poleward and thus the symmetric  
389 mixing flux of  $T$  is poleward (positive; Figs. ??a and ??b), while the down-gradient direction for  
390 tracer  $S$  is equatorward and the symmetric mixing flux of  $S$  is thus always equatorward (negative;  
391 Figs. ??c and ??d). Note that the meaning of asymmetric and symmetric mixing is very straight-  
392 forward in this setup. If there is no asymmetric mixing (green lines), the mixing flux of the  $S$  and  
393  $T$  tracers (blue lines) would be equal but opposite, meaning the amount of  $S$  tracer mixed into the  
394 troposphere would be the same as the amount of  $T$  tracer mixed into the stratosphere.

395 If we compare the magnitude of asymmetric and symmetric mixing terms for LC1 and LC2 in  
396 Fig. ??, we see that LC2 has both stronger asymmetric and symmetric mixing compared to LC1,  
397 consistent with what one might expect from Fig. ?. In both LC1 and LC2, the direction of mass  
398 flux is equatorward from the stratosphere to the troposphere (negative green lines in Figs. ??a-d),  
399 meaning the troposphere is expanding and the stratosphere is losing mass due to asymmetric mixing  
400 across the tropopause. For the tropospheric tracer  $T$ , this means that the direction of asymmetric  
401 mixing opposes the direction of symmetric mixing (Figs. ??a and ??b). Before day 4, poleward  
402 symmetric mixing of tracer  $T$  into the stratosphere dominates over the asymmetric mixing due to  
403 the large initial gradient of  $T$ . After day 4, the stratosphere has been loaded with some  $T$  tracer  
404 and the equatorward mass flux by asymmetric mixing starts to bring some of this  $T$  tracer back in  
405 to the troposphere. As a result, although LC2 exhibits stronger asymmetric and symmetric mixing,  
406 the net change in mass of  $T$  in the stratosphere ends up being similar to that of LC1 (blue lines  
407 in Figs. ??a and ??b). For the stratospheric tracer  $S$ , the directions of asymmetric and symmetric  
408 mixing are the same (Figs. ??c and ??d). After day 4, as equatorward symmetric mixing increases  
409  $S$  in the troposphere, the equatorward asymmetric mixing brings even more  $S$  tracer from the

410 stratosphere to the troposphere. As a result, LC2, with both stronger asymmetric and symmetric  
411 mixing, exhibits significantly stronger combined mixing compared to LC1.

#### 412 *Section summary*

413 We applied our new framework to quantify MLM asymmetric and symmetric mixing in the  
414 idealized lifecycle simulations of PE07. The results of this analysis can be summarized by the  
415 following two conclusions:

- 416 • the new framework is able to close the budget of tracer mass in both LC1 and LC2.
- 417 • CWB has both stronger asymmetric and symmetric mixing than AWB across an idealized  
418 tropopause.

419 In the next section, we show how the second result (and others) manifest in a full climate simula-  
420 tion.

### 421 **5. Climatology of asymmetric and symmetric mixing**

422 Figure ?? shows the climatology of potential temperature (solid line) in pressure coordinates  
423 from the idealized climate simulation. The shading denotes the range of isentropes (270K-350K)  
424 on which we quantify mixing of the idealized tracer. We further divide the shaded area into  
425 the middleworld (green shading, 300K-350K) and the underworld (pink shading, 270K-295K)  
426 (e.g. Shaw and Austin, 1930; Hoskins, 1991). The underworld is defined by isentropes that are  
427 always below the tropopause denoted by a black dashed line, while the middleworld is defined by  
428 isentropes that cross the tropopause. In the rest of the paper, the majority of the results are shown  
429 on these isentropes or as an average over the underworld or the middleworld.

430 As shown by equation (9), both asymmetric and symmetric mixing are influenced by the tracer  
431 distribution. Since the tracer setup here does not represent any specific chemical tracer in the real

432 atmosphere, it would not be generally relevant to show its mixing. Fortunately, we can readily  
 433 extract information more applicable to general situations by calculating the net mass flux (rather  
 434 than the tracer mass flux) resulting from asymmetric mixing and calculating the eddy diffusivity  
 435 to quantify symmetric mixing strength. By doing so, we factor out the influence of the specific  
 436 tracer distribution in our simulation and obtain a purely dynamical measurement of the strength of  
 437 isentropic mixing.

438 The net mass flux is calculated as  $-\frac{\partial \mathcal{M}(\dot{q})}{\partial q}$  in the asymmetric mixing term in (9). The eddy dif-  
 439 fusivity is calculated as the eddy mixing term  $\Delta \mathcal{M}(\dot{q})$  from (15) normalized by the tracer gradient  
 440 and mean mass density, that is,  $\Delta \mathcal{M}(\dot{q}) / (\bar{\sigma}^L \frac{\partial q}{\partial \phi_e})$ , where  $\bar{\sigma}^L$  is the average pseudo-density over a  
 441 tracer contour in climatological mean. Note that this expression of eddy diffusivity is very similar  
 442 to that of Chen and Plumb (2014) which employs a hybrid Eulerian-Lagrangian mean coordinate.  
 443 The difference is that they factor out the Eulerian zonal average of  $\sigma$  whereas we factor out the  
 444 Lagrangian average of  $\sigma$ . In the rest of the paper, we use mass flux to represent asymmetric mixing  
 445 strength and eddy diffusivity to represent symmetric mixing strength.

446 Note that although many studies use equivalent latitude as the coordinate, we use a tracer coordi-  
 447 nate throughout this study. However, we show our results as a function of approximate equivalent  
 448 latitude of the tracer contours to provide a geographical reference. We refer readers to Section 3c  
 449 for how we obtain the approximate equivalent latitudes.

450 The spatial pattern of the climatological eddy diffusivity is shown in Fig. ??a as a function of  
 451 approximate equivalent latitude of tracer contours, along with the jet stream (black solid contour).  
 452 In Fig ??a, eddy diffusivity minimize at the jet core near the tropopause, indicating that jet acts  
 453 as a mixing barrier (e.g. Haynes and Shuckburgh, 2000b; Chen and Plumb, 2014). The eddy  
 454 diffusivity linked to RWB bears a very similar spatial pattern to the total (Fig. ??b), and in this  
 455 model about 50% of the eddy symmetric mixing is done by large-scale RWB. The RWB frequency

456 of occurrence is plotted in grey in Fig. ??b, and agrees well with the magnitude of the eddy  
457 diffusivity, with the largest eddy diffusivities overlapping the maxima of RWB frequencies.

458 Figures ??c-d show the spatial patterns of the climatological net mass flux due to asymmetric  
459 mixing and the contribution from RWB. As discussed in Section 3b, the net mass flux due to  
460 asymmetric mixing should go toward the region of strongest symmetric mixing. Such relationship  
461 between symmetric and asymmetric mixing can be seen by comparing the eddy diffusivity and  
462 mass flux in Fig ???. The diffusivity minimizes around  $40^{\circ}N$  near the tropopause, increasing  
463 equatorward and poleward until  $60^{\circ}N$  (Fig ??a). Correspondingly, the mass flux diverges away  
464 from  $40^{\circ}N$  near the tropopause and the poleward flux stops at  $60^{\circ}N$  (Fig ??c). The large magnitude  
465 of the equatorward mass flux in the subtropics between 310K and 320K is partly due to the fact  
466 that the mass represented by these few isentropes is very large (Fig. ??). Poleward of  $60^{\circ}N$ , the  
467 diffusivity decreases with latitude and the mass is hence drawn equatorward (negative mass flux in  
468 Figs ??a and ??c). Figure ??d shows the contribution by RWB to the mass flux (shading), which  
469 resembles the total mass flux in most regions. The only exception occurs near the jet core where  
470 total mass flux is poleward while RWB mass flux is absent.

471 The RWB contribution to eddy diffusivity and mass flux is further divided into AWB contribu-  
472 tion and CWB contribution shown in Fig ?? (shading) as a function of approximate equivalent  
473 latitude, along with their corresponding frequency of occurrence (grey contours). AWB mainly  
474 occurs at lower latitudes equatorward of the jet where the mean horizontal shear of wind is anticy-  
475 clonic (Figs. ??a and ??c), while CWB mainly occurs at higher latitudes poleward of the jet where  
476 the mean shear is cyclonic (Figs. ??b and ??d). Overall, the contribution of AWB and CWB to  
477 eddy diffusivity and mass flux is proportional to their frequency of occurrence, but clearly eddy  
478 diffusivity is better coupled to wave breaking frequency.

479 A true comparison of the mass flux and eddy diffusivity between the two types of RWB can  
480 be obtained by dividing their climatological mean values by the frequency of RWB occurrence.  
481 Through this normalization, we factor out the contribution of frequency and compare the mass  
482 flux and eddy diffusivity per occurrence of AWB/CWB, i.e. their efficiency. In the most of the  
483 underworld, AWB and CWB related mass flux has the same sign and comparable efficiency (not  
484 shown), that is, a single occurrence causes the same mass flux. In the middleworld between  $45^{\circ}N$   
485 and  $60^{\circ}N$ , AWB and CWB have opposite signed mass flux. Specifically, between  $45^{\circ}N$  and  $60^{\circ}N$ ,  
486 AWB exhibits equatorward mass flux and CWB exhibits poleward mass flux across the tropopause  
487 (Figs. ??c and ??d).

488 The comparison of eddy diffusivity per occurrence for the two types of RWB is shown in Figs.  
489 ??c and ??d as a function of approximate equivalent latitude, along with their counterparts in the  
490 idealized eddy lifecycle shown in Figs. ??a and ??b. In both the lifecycle and climate simulations,  
491 CWB (LC2) exhibits a larger diffusivity than AWB (LC1) in the midlatitudes. The difference is  
492 especially evident in the climate simulation near  $50^{\circ}N$  equivalent latitude (Figs. ??c and ??d).  
493 Recall that the lifecycle simulations are only made of one event, while the climate simulation  
494 is composed of thousands. Thus, we do not expect the results to be identical. However, the  
495 lifecycle simulations bear much resemblance to the climate simulations in Fig. ??, indicating the  
496 relevance of the idealized lifecycle simulations to more realistic climate settings. Interestingly,  
497 they also agree on the existence of negative eddy diffusivity equatorward of the jet stream in the  
498 subtropics linked to CWB (Figs. ??b and ??d). Note such negative diffusivity might be an artifact  
499 arising from the hyperdiffusion used in our model. In addition, as discussed in Section 3d, the  
500 negative diffusivity in Fig. ??d could also arise from the fact that local contribution to the eddy  
501 diffusivity is not guaranteed to be positive. Nevertheless, such up-gradient mixing behavior has  
502 been documented in reanalysis data within a similar latitude range (Birner et al., 2013), and more

503 study is needed to tell whether the negative eddy diffusivity linked to CWB in Fig. 7 is an artifact  
504 or has physical implications.

### 505 *Section summary*

506 We quantify the climatology of asymmetric and symmetric mixing, quantified by net mass flux  
507 and eddy diffusivity in a climate simulation and find,

- 508 • CWB has a comparable asymmetric mixing efficiency (net mass flux) but significantly  
509 stronger symmetric mixing efficiency (eddy diffusivity) than AWB in the underworld,
- 510 • the eddy diffusivity in lifecycle simulations bears resemblance to that in the climate simula-  
511 tions.

512 In the next section, we show how such differences in RWB symmetric mixing efficiency translate  
513 into a dependence of total symmetric mixing on jet variability.

## 514 **6. Dependence on jet stream variability**

515 The dependence of asymmetric and symmetric mixing on the internal variability of the jet,  
516 specifically the latitudinal shifts of jet, is explored by compositing the mass flux and eddy diffu-  
517 sivity with respect to various jet latitudes. We calculate the jet latitude as the latitude of maximum  
518 850hPa zonal-mean zonal wind at 6-hour resolution (e.g. Barnes and Hartmann, 2010; ?). We  
519 group the jet latitudes into four bins centered at  $39^\circ N$ ,  $43^\circ N$ ,  $47^\circ N$ , and  $51^\circ N$ . These latitudes are  
520 chosen to make each bin have a similar sample size. We then composite RWB frequency, total  
521 mass flux and eddy diffusivity, and the contribution by RWB according to these jet latitude bins.

522 *a. Tropospheric asymmetric and symmetric mixing*

523 The tropospheric asymmetric and symmetric mixing are investigated by focusing on the under-  
524 world, which constitutes a corridor between the midlatitude boundary layer and the polar middle-  
525 to-upper troposphere (Fig. ??). The average frequency of RWB in this corridor is shown in Fig.  
526 ?? as a function of approximate equivalent latitude. Consistent with previous studies, AWB occurs  
527 more frequently while CWB occurs less frequently as the jet moves poleward. The extent of the  
528 frequency change associated with AWB and CWB are comparable in midlatitudes around  $45^{\circ}N$ .  
529 This indicates the compensation between the two types of RWB when jet shifts around, keeping  
530 RWB frequency relatively constant in the midlatitudes (Fig. ??c).

531 Figure ?? shows the composite mass flux due to asymmetric mixing and the contribution from  
532 RWB as a function of approximate equivalent latitude for various jet latitudes. RWB contributes  
533 less than 20% of the total mass flux in the subtropics and about 50% poleward of  $55^{\circ}N$  equivalent  
534 latitude. Neither total mass flux nor RWB contribution show significant change when the jet  
535 wobbles around (Figs. ??a and ??b). At least for the RWB contribution, this is due to the opposing  
536 changes in frequency of AWB and CWB (Figs. ??a and ??b), combined with the fact that the  
537 two types have comparable asymmetric mixing efficiencies in the underworld. As a result, the  
538 change in mass flux associated with AWB and CWB largely cancel each other (Figs. ??c and ??d)  
539 and leave the RWB mass flux largely unchanged (Fig. ??b). In this case, the mass flux in the  
540 underworld does not rely heavily on the jet latitude.

541 Figures ??a and ??b show the total eddy diffusivity and the contribution from RWB as a function  
542 of approximate equivalent latitude. RWB contributes slightly more than half of the total and both  
543 the total and RWB contribution to eddy diffusivity decrease when the jet is more poleward, in  
544 contrast to the case of mass flux. The difference lies in the fact that CWB has a significantly

545 stronger eddy diffusivity than AWB (Figs. ??c and ??d). As a result, the decrease in CWB  
546 diffusivity overwhelms the increase in AWB diffusivity although their changes in the frequency  
547 of occurrence are comparable (Fig. ??). This effect is most evident in the midlatitudes around  
548  $45^{\circ}N$  equivalent latitude. In this case, the difference between AWB and CWB symmetric mixing  
549 efficiency is key to determining the change in total eddy diffusivity linked with changes in the jet  
550 position.

### 551 *b. Stratosphere-troposphere exchange (STE)*

552 As shown in Fig. ??, RWB promotes STE by distorting the tropopause. The vertical distortion  
553 of the tropopause by AWB and CWB in the idealized lifecycle simulations is demonstrated in Fig.  
554 ?? by snapshots on day 6 and day 7 respectively. The two dates are chosen for the peak stage  
555 of AWB and CWB mixing (Fig. ??). In Fig. ??, both AWB and CWB are associated with an  
556 intrusion of stratospheric air that extends as low as 850hPa. These streamers are also observed  
557 in nature (e.g. Shapiro, 1980) and are responsible for injecting anthropogenic pollutants into the  
558 stratosphere and bringing ozone-rich stratospheric air down to the boundary layer. Quantifying  
559 the variability of RWB-related STE as shown in Fig. ?? is hence of great interest. To serve this  
560 purpose, the tropopause is first defined as the tracer contour whose mean position is closest to  
561 the 2PVU surface for the four jet latitudes. Then composite mass flux and eddy diffusivity are  
562 extracted along the corresponding tropopauses for the four jet latitudes.

563 The composite frequencies of occurrence of the two types of RWB in the middleworld are shown  
564 in Fig. ?? with respect to jet latitude. AWB mainly occurs equatorward of the jet while CWB  
565 mainly occurs poleward of the jet and there is little overlap. When the jet shifts poleward, AWB  
566 occurs more frequently while CWB occurs less frequently. Figures ??a and ??b show the total  
567 mass flux across the tropopause due to asymmetric mixing and the contribution from RWB. Both

568 the total and RWB contribution exhibit troposphere-to-stratosphere mass flux equatorward of  $55^{\circ}\text{N}$   
569 equivalent latitude and stratosphere-to-troposphere mass flux poleward of  $55^{\circ}\text{N}$ . In terms of the  
570 variability associated with the jet shifting, a substantial portion of the total can be explained by the  
571 RWB contribution (compare Figs. ??a and ??b), which in turn, is dominated by the CWB con-  
572 tribution (Fig. ??c). Such dominance is largely due to the stronger decrease in CWB frequency  
573 compared to the increase in AWB frequency (Fig. ??). As such, the total mass flux across the  
574 tropopause shifts poleward and weakens as the jet shifts poleward. Due to the same line of reason-  
575 ing, the variability of eddy diffusivity along the tropopause is also dominated by the changes in  
576 CWB (Fig. ??). The maximum eddy diffusivity moves poleward and weakens as the jet shifts pole-  
577 ward. While AWB and CWB do exhibit different symmetric mixing efficiencies, these changes  
578 are predominantly explained by changes in RWB frequency itself.

### 579 *c. Section summary*

580 As the jet shifts poleward,

- 581 • underworld mass flux due to asymmetric mixing does not change due to the compensating  
582 frequency changes of AWB and CWB, and their similar asymmetric mixing efficiencies.
- 583 • underworld eddy diffusivity (symmetric mixing strength) decreases due to the difference in  
584 AWB and CWB symmetric mixing efficiencies.
- 585 • across the tropopause, both mass flux due to asymmetric mixing and eddy diffusivity that  
586 represents symmetric mixing decrease due to the dominant decrease in CWB frequency.

## 587 7. Conclusions

588 A new framework to quantify both asymmetric and symmetric isentropic mixing is proposed  
589 and applied to Rossby wave breaking (RWB) in both free eddy lifecycle simulations and a forced  
590 climate simulation. The focus of this study is on the difference between the two flavors of RWB  
591 – anticyclonic wave breaking (AWB) and cyclonic wave breaking (CWB). It is found that in both  
592 sets of simulations and throughout different regions of the atmosphere, CWB has either compa-  
593 rable or stronger isentropic mixing than AWB. This result has implications for the influence of  
594 climate variability on isentropic mixing. Since CWB occurs less frequently and AWB occurs  
595 more frequently as the jet shifts poleward, mixing differences translate into a decrease in symmet-  
596 ric mixing strength (eddy diffusivity) within the troposphere, and decrease in both symmetric and  
597 asymmetric mixing (net mass flux) across the tropopause, as the jet shifts poleward.

598 Although the simulations in this study are highly idealized, we argue that the conclusions ob-  
599 tained are applicable to the real atmosphere. Abalos et al. (2016) used ERA-Interim to show that in  
600 winter the effective diffusivity across the tropopause decreases in the mid-to-high latitudes during  
601 a positive Northern Annular Mode when the jet is more poleward, and increases during positive  
602 ENSO when the jet is more equatorward. These results are consistent with the modulation of the  
603 jet stream on the two types of RWB. Although our study does not directly address the jet shift in  
604 response to external forcing (e.g. anthropogenic climate change), we expect similar results to what  
605 is found here due to the same relationship between RWB and the jet stream in climate change sim-  
606 ulations (e.g. Barnes and Polvani, 2013). In fact, Orbe et al. (2015) demonstrated that isentropic  
607 mixing from the midlatitude boundary layer to the Arctic increases over the northeast Pacific with  
608 climate change in a state-of-the-art GCM where the jet stream shifts equatorward. This is con-

609 sistent with our argument that an equatorward jet shift increases the frequency of cyclonic wave  
 610 breaking, and thus, increases the high-latitude mixing strength.

611 In the real atmosphere, certain constituents whose spatial distributions are subject to climate  
 612 change, also contribute to the climate forcing. Examples include carbon dioxide, ozone, various  
 613 species of aerosols and water vapor. Understanding the passive response of atmospheric con-  
 614 stituents to climate change is thus an important step towards understanding the entire feedback  
 615 loop. This study provides a quantification methodology and a mechanistic explanation for how the  
 616 isentropic mixing of constituents may respond to future jet shifts.

617 *Acknowledgments.* This work was supported by the Climate and Large-scale Dynamics Program  
 618 of the National Science Foundation under Grant 1419818.

## 619 APPENDIX A

### 620 Derivation of modified Lagrangian mean (MLM) tracer equation

621 Taking inspiration from Nakamura (1995), we show that the derivation of MLM tracer equation  
 622 is to a large extent a mathematical transformation that starts with:

$$\frac{\partial \mathcal{M}(\chi)}{\partial t} = \frac{\partial}{\partial t} \iint_{q^* \leq q} \sigma \chi dA = \iint_{q^* \leq q} \frac{\partial(\sigma \chi)}{\partial t} dA - \frac{\partial}{\partial q} \iint_{q^* \leq q} \sigma \chi \frac{\partial q^*}{\partial t} dA \quad (\text{A1})$$

623 The only physics that comes in is that of mass conservation:

$$\frac{\partial(\sigma \chi)}{\partial t} = -\nabla_{\theta} \cdot (\sigma \chi \mathbf{u}) - \frac{\partial(\sigma \chi \dot{\theta})}{\partial \theta} + \sigma \dot{\chi} \quad (\text{A2})$$

$$\frac{\partial q^*}{\partial t} = -\mathbf{u} \cdot \nabla_{\theta} q^* - \dot{\theta} \frac{\partial q^*}{\partial \theta} + \dot{q}^* \quad (\text{A3})$$

625 where  $\dot{\chi}$  and  $q^*$  represent non-conservative processes such as diffusion and/or production of the  
 626 two tracers. Substituting (A2) and (A3) into (A1) and re-arranging,

$$\begin{aligned} \frac{\partial \mathcal{M}(\chi)}{\partial t} = & - \iint_{q^* \leq q} \nabla_{\theta} \cdot (\sigma \chi \mathbf{u}) dA + \frac{\partial}{\partial q} \iint_{q^* \leq q} \sigma \chi \mathbf{u} \cdot \nabla_{\theta} q^* dA + \frac{\partial}{\partial q} \iint_{q^* \leq q} \sigma \chi \dot{\theta} \frac{\partial q^*}{\partial \theta} dA \\ & - \iint_{q^* \leq q} \frac{\partial (\sigma \chi \dot{\theta})}{\partial \theta} dA - \frac{\partial}{\partial q} \iint_{q^* \leq q} \sigma \chi \dot{q}^* dA + \iint_{q^* \leq q} \sigma \dot{\chi} dA \end{aligned} \quad (\text{A4})$$

627 Applying the divergence theorem to the first term on the *rhs* of (A4) and using the relation (6b)  
 628 leads to:

$$- \iint_{q^* \leq q} \nabla_{\theta} \cdot (\sigma \chi \mathbf{u}) dA = - \oint_{q^*=q} \sigma \chi \mathbf{u} \cdot \frac{\nabla_{\theta} q^*}{|\nabla_{\theta} q^*|} dl = - \frac{\partial}{\partial q} \iint_{q^* \leq q} \sigma \chi \mathbf{u} \cdot \nabla_{\theta} q dA \quad (\text{A5})$$

629 Substituting (A5) into (A4) and noting that:

$$\frac{\partial}{\partial q} \iint_{q^* \leq q} \sigma \chi \dot{\theta} \frac{\partial q^*}{\partial \theta} dA - \iint_{q^* \leq q} \frac{\partial (\sigma \chi \dot{\theta})}{\partial \theta} dA = - \frac{\partial}{\partial \theta} \iint_{q^* \leq q} \sigma \chi \dot{\theta} dA \quad (\text{A6})$$

630 one obtains:

$$\begin{aligned} \frac{\partial \mathcal{M}(\chi)}{\partial t} = & - \frac{\partial}{\partial q} \iint_{q^* \leq q} \sigma \chi \dot{q}^* dA - \frac{\partial}{\partial \theta} \iint_{q^* \leq q} \sigma \chi \dot{\theta} dA + \iint_{q^* \leq q} \sigma \dot{\chi} dA \\ = & - \frac{\partial \mathcal{M}(\dot{q}\chi)}{\partial q} - \frac{\partial \mathcal{M}(\dot{\theta}\chi)}{\partial \theta} + \mathcal{M}(\dot{\chi}) \end{aligned} \quad (\text{A7})$$

## 631 APPENDIX B

### 632 Derivation of effective diffusivity

633 Instead of assuming (10), we assume a more general form of hyperdiffusion for 2-D flow:

$$\dot{q} = \kappa \nabla^{2m} q = \kappa \nabla \cdot \nabla (\nabla^{2(m-1)} q) \quad (\text{B1})$$

634 where (10) is the special case in which  $m = 1$ . Plugging (B1) into  $\mathcal{M}(\dot{q})$  leads to:

$$\mathcal{M}(\dot{q}) = \sigma_0 \kappa \iint_{q^* \leq q} \nabla \cdot \nabla (\nabla^{2(m-1)} q^*) dA$$

635 Using the divergence theorem,

$$\mathcal{M}(\dot{q}) = \sigma_0 \kappa \oint_{q^*=q} \nabla(\nabla^{2(m-1)} q^*) \cdot \frac{\nabla q^*}{|\nabla q^*|} dl$$

636 and using relation (6b):

$$\begin{aligned} \mathcal{M}(\dot{q}) &= \sigma_0 \kappa \frac{\partial}{\partial q} \iint \nabla(\nabla^{2(m-1)} q^*) \cdot \nabla q^* dl \\ &= \sigma_0 \kappa \frac{\partial}{\partial A} \iint \nabla(\nabla^{2(m-1)} q^*) \cdot \nabla q^* dl \frac{\partial A}{\partial q} \\ &= \sigma_0 \kappa \underbrace{\frac{\frac{\partial}{\partial A} \iint \nabla(\nabla^{2(m-1)} q^*) \cdot \nabla q^* dl}{(\frac{\partial q}{\partial A})^2}}_{\kappa_{eff}} \frac{\partial q}{\partial A} \end{aligned} \quad (\text{B2})$$

637 This form of effective diffusivity  $\kappa_{eff}$  is identical to that in Nakamura and Zhu (2010) (appendix  
638 D). Letting  $m = 1$ ,  $\kappa_{eff}$  takes the form of (13) which is identical to that in Nakamura (1996). Note  
639 that we could use (B2) to calculate the symmetric mixing term  $\mathcal{M}(\dot{q})$  since in our model  $\dot{q}$  does  
640 take a hyperdiffusion form. However, we choose to directly integrate the small-scale diffusion  $\dot{q}$   
641 to be consistent with our calculation of the asymmetric mixing term  $-q \partial \mathcal{M}(\dot{q}) / \partial q$ .

## 642 References

643 Abalos, M., B. Legras, and E. Shuckburgh, 2016: Interannual variability in effective diffusivity in  
644 the upper troposphere/lower stratosphere from reanalysis data. *Quarterly Journal of the Royal*  
645 *Meteorological Society*, **142 (697)**, 1847–1861.

646 Appenzeller, C., H. Davies, and W. Norton, 1996: Fragmentation of stratospheric intrusions. *J.*  
647 *Geophys. Res.*, **101 (D1)**, 1435–1456.

648 Appenzeller, C., and H. C. Davies, 1992: Structure of stratospheric intrusions into the troposphere.  
649 *Nature*, **358 (6387)**, 570–572, URL <http://dx.doi.org/10.1038/358570a0>.

- 650 Barnes, E. A., and D. L. Hartmann, 2010: Influence of eddy-driven jet latitude on north atlantic  
651 jet persistence and blocking frequency in cmip3 integrations. *Geophysical Research Letters*,  
652 **37 (23)**, doi:10.1029/2010GL045700, URL <http://dx.doi.org/10.1029/2010GL045700>, 123802.
- 653 Barnes, E. A., and D. L. Hartmann, 2012: Detection of rossby wave breaking and its response  
654 to shifts of the midlatitude jet with climate change. *Journal of Geophysical Research: Atmo-*  
655 *spheres*, **117 (D9)**, doi:10.1029/2012JD017469, URL <http://dx.doi.org/10.1029/2012JD017469>,  
656 d09117.
- 657 Barnes, E. A., and L. Polvani, 2013: Response of the midlatitude jets, and of their variability, to  
658 increased greenhouse gases in the CMIP5 models. *Journal of Climate*, **26 (18)**, 7117–7135.
- 659 Barrie, L. A., 1986: Arctic air pollution: an overview of current knowledge. *Atmospheric Envi-*  
660 *ronment (1967)*, **20 (4)**, 643–663.
- 661 Birner, T., D. J Thompson, and T. Shepherd, 2013: Up-gradient eddy fluxes of potential vorticity  
662 near the subtropical jet. *Geophys. Res. Lett.*, **40 (22)**, 5988–5993.
- 663 Butchart, N., and E. E. Remsberg, 1986: The area of the stratospheric polar vortex as a diagnostic  
664 for tracer transport on an isentropic surface. *J. Atmos. Sci.*, **43 (13)**, 1319–1339.
- 665 Butler, A. H., D. W. Thompson, and R. Heikes, 2010: The steady-state atmospheric circulation  
666 response to climate change-like thermal forcings in a simple general circulation model. *Journal*  
667 *of Climate*, **23 (13)**, 3474–3496.
- 668 Chen, G., and A. Plumb, 2014: Effective isentropic diffusivity of tropospheric transport. *J. Atmos.*  
669 *Sci.*, **71 (9)**, 3499–3520.
- 670 Chen, P., 1995: Isentropic cross-tropopause mass exchange in the extratropics. *J. Geophys. Res.*,  
671 **100 (D8)**, 16 661–16 673.

672 Chen, W. Y., and H. M. van den Dool, 1999: Significant change of extratropical natural variability  
673 and potential predictability associated with the El Nino/Southern Oscillation. *Tellus A*, **51 (5)**,  
674 790–802.

675 Eckhardt, S., A. Stohl, H. Wernli, P. James, C. Forster, and N. Spichtinger, 2004: A 15-year  
676 climatology of warm conveyor belts. *Journal of climate*, **17 (1)**, 218–237.

677 Edouard, S., R. Vautard, and G. Brunet, 1997: On the maintenance of potential vorticity in isen-  
678 tropic coordinates. *Quart. J. Roy. Meteorol. Soc.*, **123 (543)**, 2069–2094.

679 Haynes, P., and E. Shuckburgh, 2000a: Effective diffusivity as a diagnostic of atmospheric trans-  
680 port: 1. stratosphere. *J. Geophys. Res.*, **105 (D18)**, 22 777–22 794.

681 Haynes, P., and E. Shuckburgh, 2000b: Effective diffusivity as a diagnostic of atmospheric trans-  
682 port: 2. troposphere and lower stratosphere. *J. Geophys. Res.*, **105 (D18)**, 22 795–22 810, doi:  
683 10.1029/2000JD900092, URL <http://dx.doi.org/10.1029/2000JD900092>.

684 Held, I. M., and M. J. Suarez, 1994: A proposal for the intercomparison of the dynamical cores of  
685 atmospheric general circulation models. *Bull. Amer. Meteor. Soc.*, **75 (10)**, 1825–1830.

686 Holton, J. R., P. H. Haynes, M. E. McIntyre, A. R. Douglass, R. B. Rood, and L. Pfister, 1995:  
687 Stratosphere-troposphere exchange. *Reviews of Geophysics*, **33 (4)**, 403–439.

688 Hoskins, B. J., 1991: Towards a PV- $\theta$  view of the general circulation. *Tellus A*, **43 (4)**, 27–35.

689 Jing, P., D. Cunnold, H. Wang, and E. Yang, 2004: Isentropic cross-tropopause ozone transport in  
690 the northern hemisphere. *J. Atmos. Sci.*, **61 (9)**, 1068–1078.

691 Leibensperger, E. M., and R. A. Plumb, 2014: Effective diffusivity in baroclinic flow. *Journal of*  
692 *the Atmospheric Sciences*, **71 (3)**, 972–984.

693 Lelieveld, J., and F. J. Dentener, 2000: What controls tropospheric ozone? *J. Geophys. Res.*,  
694 **105 (D3)**, 3531–3551.

695 Lippmann, M., 1989: Health effects of ozone a critical review. *Japca*, **39 (5)**, 672–695.

696 Liu, C., and E. A. Barnes, 2015: Extreme moisture transport into the Arctic linked to Rossby wave  
697 breaking. *J. Geophys. Res.*, **120 (9)**, 3774–3788.

698 Liu, C., X. Ren, and X. Yang, 2014: Mean flow-storm track relationship and Rossby wave breaking  
699 in two types of El-Niño. *Adv. Atmos. Sci.*, **31 (1)**, 197–210.

700 Madonna, E., H. Wernli, H. Joos, and O. Martius, 2014: Warm conveyor belts in the ERA-Interim  
701 dataset (1979–2010). Part I: Climatology and potential vorticity evolution. *J. Climate*, **27 (1)**,  
702 3–26.

703 McIntyre, M., 1980: Towards a lagrangian-mean description of stratospheric circulations and  
704 chemical transports. *Philosophical Transactions of the Royal Society of London A: Mathematical,*  
705 *Physical and Engineering Sciences*, **296 (1418)**, 129–148.

706 Nakamura, N., 1995: Modified lagrangian-mean diagnostics of the stratospheric polar vortices.  
707 part I. Formulation and analysis of GFDL SKYHI GCM. *J. Atmos. Sci.*, **52 (11)**, 2096–2108.

708 Nakamura, N., 1996: Two-dimensional mixing, edge formation, and permeability diagnosed in an  
709 area coordinate. *J. Atmos. Sci.*, **53 (11)**, 1524–1537.

710 Nakamura, N., 2004: Quantifying asymmetric wave breaking and two-way transport. *J. Atmos.*  
711 *Sci.*, **61 (22)**, 2735–2748.

712 Nakamura, N., 2007: Extratropical stratosphere-troposphere mass exchange associated with isen-  
713 tropic mixing: A 1992–2005 climatology derived from advection-diffusion calculations. *J. Geo-*  
714 *phys. Res.*, **112 (D24)**.

- 715 Nakamura, N., and D. Zhu, 2010: Finite-amplitude wave activity and diffusive flux of potential  
716 vorticity in eddy-mean flow interaction. *J. Atmos. Sci.*, **67** (9), 2701–2716.
- 717 Orbe, C., P. A. Newman, D. W. Waugh, M. Holzer, L. D. Oman, F. Li, and L. M. Polvani, 2015:  
718 Air-mass origin in the Arctic. Part II: Response to increases in greenhouse gases. *J. Climate*,  
719 **28** (23), 9105–9120.
- 720 Pan, L. L., and Coauthors, 2009: Tropospheric intrusions associated with the secondary  
721 tropopause. *Journal of Geophysical Research: Atmospheres*, **114** (D10), doi:10.1029/  
722 2008JD011374, URL <http://dx.doi.org/10.1029/2008JD011374>, d10302.
- 723 Polvani, L. M., and J. G. Esler, 2007: Transport and mixing of chemical air masses in idealized  
724 baroclinic life cycles. *Journal of Geophysical Research: Atmospheres*, **112** (D23), doi:10.1029/  
725 2007JD008555, URL <http://dx.doi.org/10.1029/2007JD008555>, d23102.
- 726 Raatz, W. E., and G. E. Shaw, 1984: Long-range tropospheric transport of pollution aerosols into  
727 the alaskan arctic. *Journal of Climate and Applied Meteorology*, **23** (7), 1052–1064.
- 728 Randel, W. J., D. J. Seidel, and L. L. Pan, 2007: Observational characteristics of dou-  
729 ble tropopauses. *Journal of Geophysical Research: Atmospheres*, **112** (D7), doi:10.1029/  
730 2006JD007904, URL <http://dx.doi.org/10.1029/2006JD007904>, d07309.
- 731 Rasmusson, E. M., and J. M. Wallace, 1983: Meteorological aspects of the El Nino/Southern  
732 Oscillation. *Science*, **222** (4629), 1195–1202.
- 733 Ren, X., Y. Zhang, and Y. Xiang, 2008: Connections between wintertime jet stream variability,  
734 oceanic surface heating, and transient eddy activity in the north pacific. *Journal of Geophysi-  
735 cal Research: Atmospheres*, **113** (D21), doi:10.1029/2007JD009464, URL [http://dx.doi.org/10.  
736 1029/2007JD009464](http://dx.doi.org/10.1029/2007JD009464), d21119.

- 737 Rivière, G., 2011: A dynamical interpretation of the poleward shift of the jet streams in global  
738 warming scenarios. *J. Atmos. Sci.*, **68 (6)**, 1253–1272.
- 739 Shapiro, M., 1980: Turbulent mixing within tropopause folds as a mechanism for the exchange  
740 of chemical constituents between the stratosphere and troposphere. *J. Atmos. Sci.*, **37 (5)**, 994–  
741 1004.
- 742 Shaw, N., and E. Austin, 1930: Manual of meteorology, vol. 3: the physical processes of weather.  
743 Cambridge University Press.
- 744 Strong, C., and G. Magnusdottir, 2008: Tropospheric Rossby wave breaking and the NAO/NAM.  
745 *J. Atmos. Sci.*, **65 (9)**, 2861–2876.
- 746 Thompson, D. W., and S. Solomon, 2002: Interpretation of recent southern hemisphere climate  
747 change. *Science*, **296 (5569)**, 895–899.
- 748 Thorncroft, C., B. Hoskins, and M. McIntyre, 1993: Two paradigms of baroclinic-wave life-cycle  
749 behaviour. *Quart. J. Roy. Meteorol. Soc.*, **119 (509)**, 17–55.
- 750 Trepte, C. R., R. E. Veiga, and M. P. McCormick, 1993: The poleward dispersal of mount pinatubo  
751 volcanic aerosol. *J. Geophys. Res.*, **98 (D10)**, 18 563–18 573.
- 752 Wang, S., and L. M. Polvani, 2011: Double tropopause formation in idealized baroclinic life  
753 cycles: The key role of an initial tropopause inversion layer. *Journal of Geophysical Re-  
754 search: Atmospheres*, **116 (D5)**, doi:10.1029/2010JD015118, URL [http://dx.doi.org/10.1029/  
755 2010JD015118](http://dx.doi.org/10.1029/2010JD015118), d05108.
- 756 Woollings, T., A. Hannachi, and B. Hoskins, 2010: Variability of the North Atlantic eddy-driven  
757 jet stream. *Quarterly Journal of the Royal Meteorological Society*, **136 (649)**, 856–868.

- 758 Woollings, T., B. Hoskins, M. Blackburn, and P. Berrisford, 2008: A new Rossby wave-breaking  
759 interpretation of the North Atlantic Oscillation. *J. Atmos. Sci.*, **65** (2), 609–626.
- 760 Yang, H., G. Chen, and D. I. Domeisen, 2014: Sensitivities of the lower-stratospheric transport  
761 and mixing to tropical SST heating. *J. Atmos. Sci.*, **71** (7), 2674–2694.
- 762 Yang, H., G. Chen, Q. Tang, and P. Hess, 2016: Quantifying isentropic stratosphere-troposphere  
763 exchange of ozone. *Journal of Geophysical Research: Atmospheres*, **121** (7), 3372–3387, doi:  
764 10.1002/2015JD024180, URL <http://dx.doi.org/10.1002/2015JD024180>, 2015JD024180.



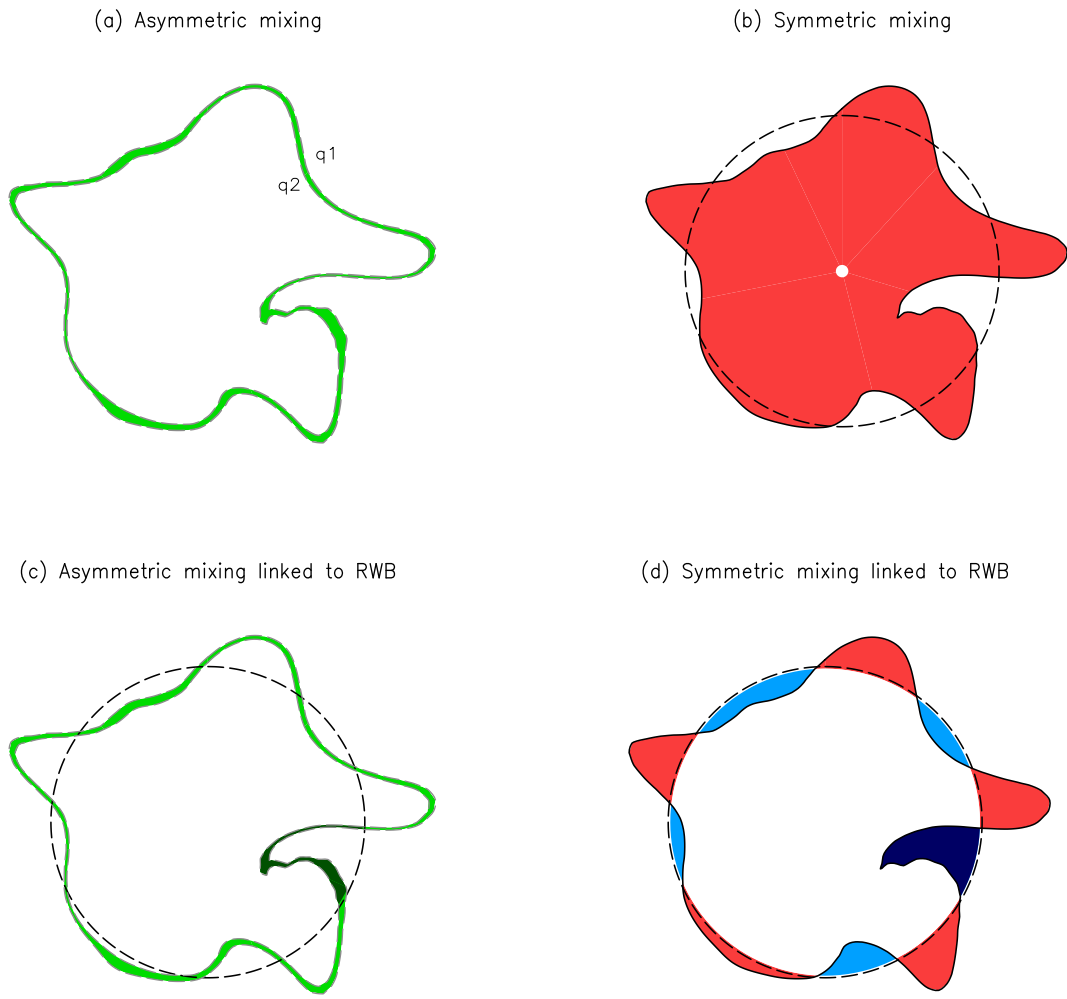


FIG. 1: Schematics depicting the integration area for the asymmetric mixing (left) and symmetric mixing (right) terms. (a) and (b) illustrate the calculation of total asymmetric and symmetric mixing. (c) illustrates the asymmetric mixing related to Rossby wave breaking (dark green), and (d) illustrates the symmetric mixing by waves (all shading), and the part related to Rossby wave breaking (dark blue shading). See text for additional details.

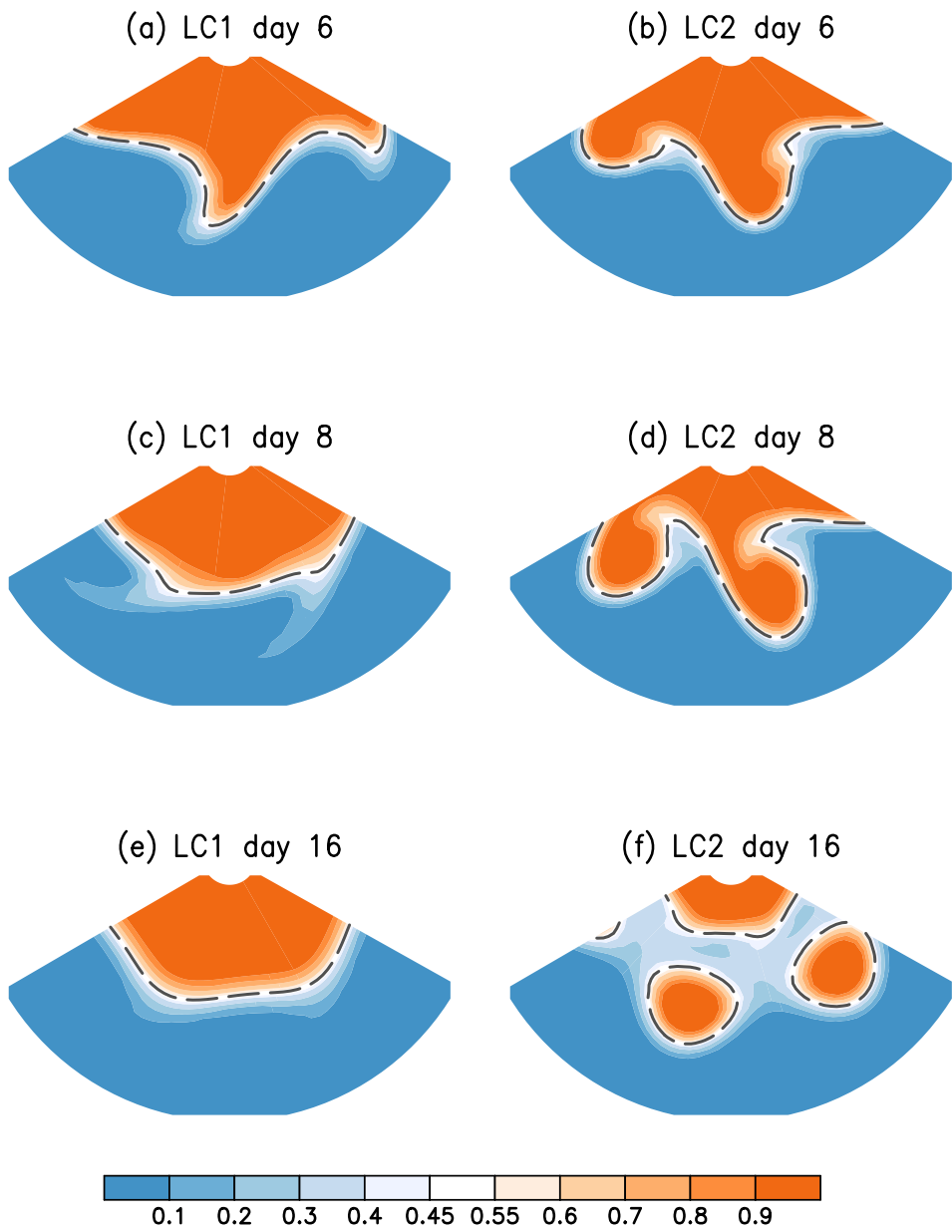
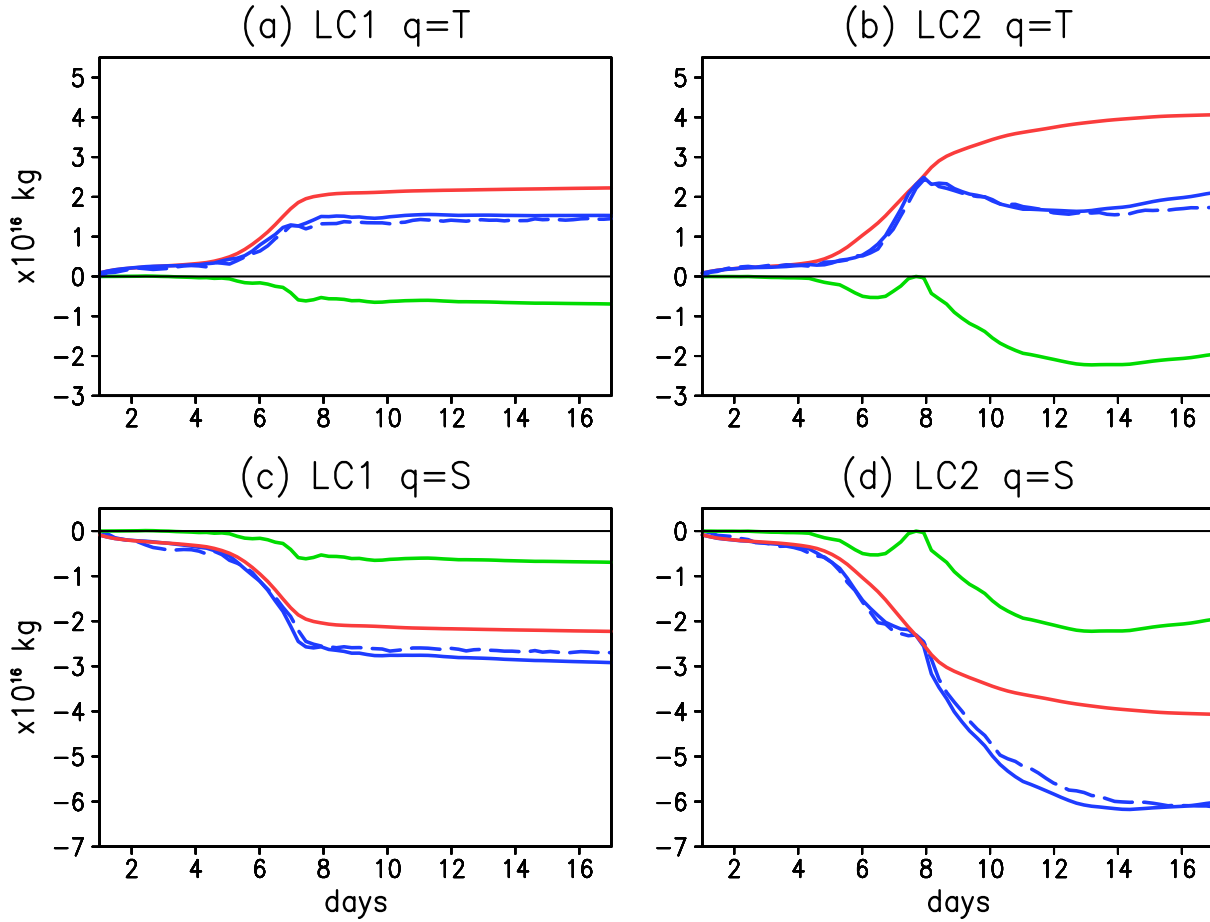


FIG. 2: Snapshots of the concentration of the stratospheric tracer (shading) on the 335K isentropes in the idealized LC1 (left column) and LC2 (right columns) simulations. Dashed contours denote the tropopause defined as the 0.5 contour of the stratospheric tracer.



$$\mathcal{M}(q) \Big|_{t_0}^t = - \int_{t_0}^t q \frac{\partial \mathcal{M}(\dot{q})}{\partial q} dt + \int_{t_0}^t \mathcal{M}(\dot{q}) dt$$

FIG. 3: Time integration of asymmetric mixing (green) and symmetric mixing (red) of tracer  $T$  and  $S$  for LC1 and LC2 simulations (unit:  $1 \times 10^{16}$  kg). Dashed blue lines denote the actual change in tracer mass due to mixing, with the solid blue lines denoting that estimated by the sum of the asymmetric and symmetric mixing terms (solid blue = solid red + solid green). Positive (negative) values denote a poleward (equatorward) mixing into the stratosphere (troposphere).

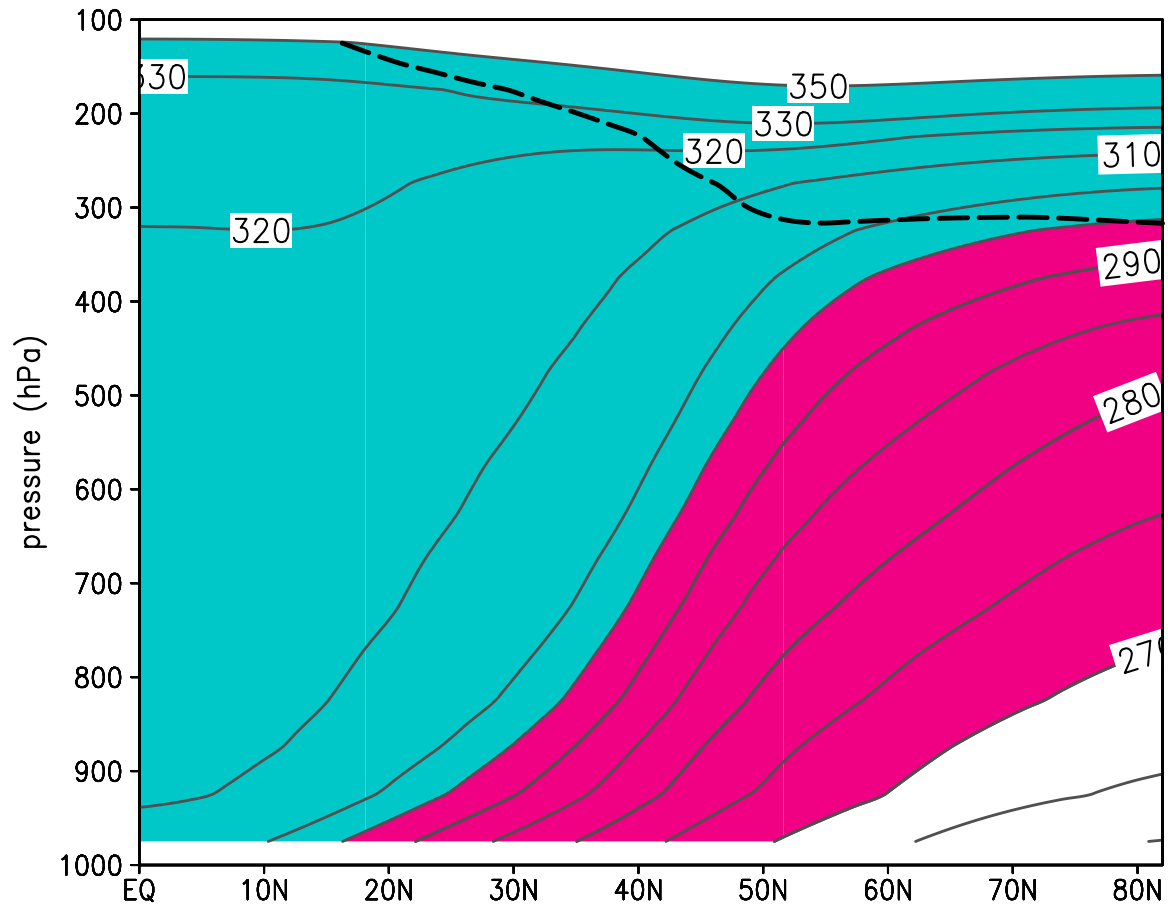


FIG. 4: Climatology of zonal-mean potential temperature  $\theta$  in the 25-year climate run (solid contours, unit: K). The dashed line denotes the climatological 2 PVU surface which represents the dynamical tropopause. Pink and light green shading denote the underworld and the middleworld analyzed here.

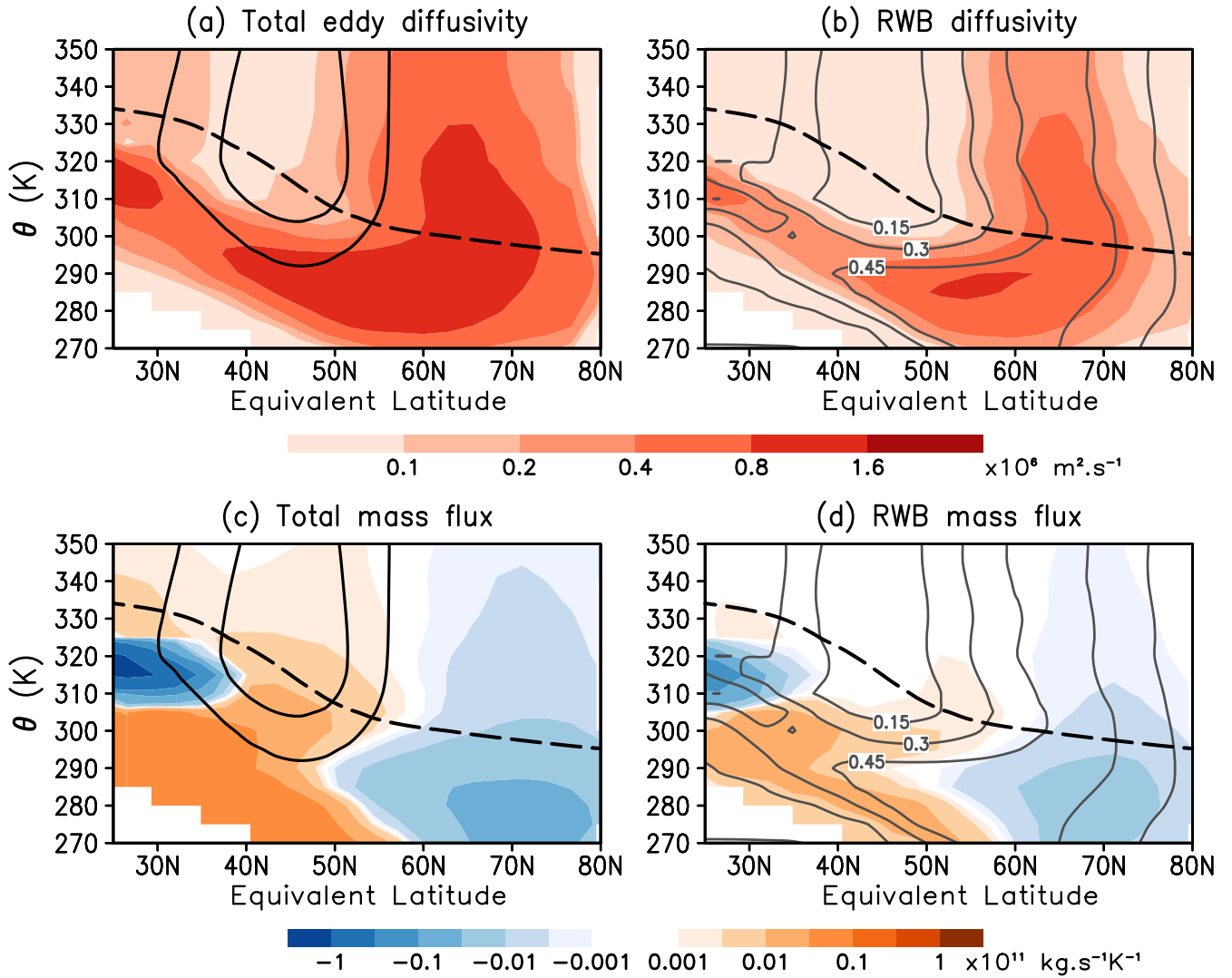


FIG. 5: **Upper row:** Climatology of eddy diffusivity (shading) as a function of approximate equivalent latitude of the tracer contours for the (a) total, (b) Rossby wave breaking (RWB) contribution. **Lower row:** The same as the upper row, but for net mass flux due to asymmetric mixing. The two solid black contours in the left column denote the 20m/s and 30m/s contours of the zonal mean zonal wind. Contours in the right column denote the frequency of occurrence of RWB events. The black dashed line is the 2PVU contour that represents the dynamical tropopause.

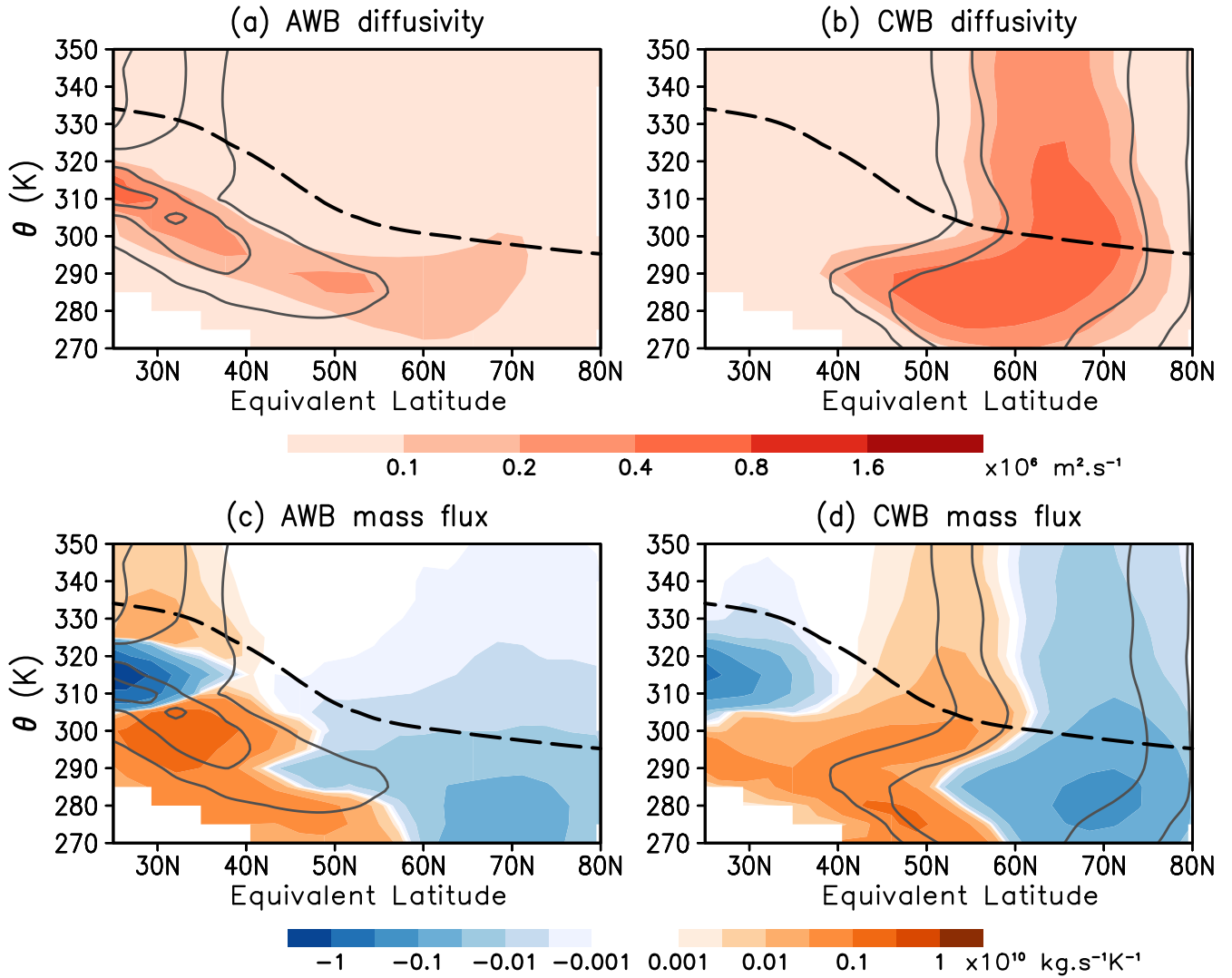


FIG. 6: **Upper row:** Contribution of (a) anticyclonic wave breaking (AWB) contribution, and (b) cyclonic wave breaking (CWB) to eddy diffusivity (shading) as a function of approximate equivalent latitude of the coordinate contours. **Lower row:** The same as the upper row, but for net mass flux due to asymmetric mixing. Solid grey contours denote the frequency of occurrence of AWB in the left column and CWB in the right column, with a contour interval of 0.15. The black dashed line is the 2PVU contour that represents the dynamical tropopause.

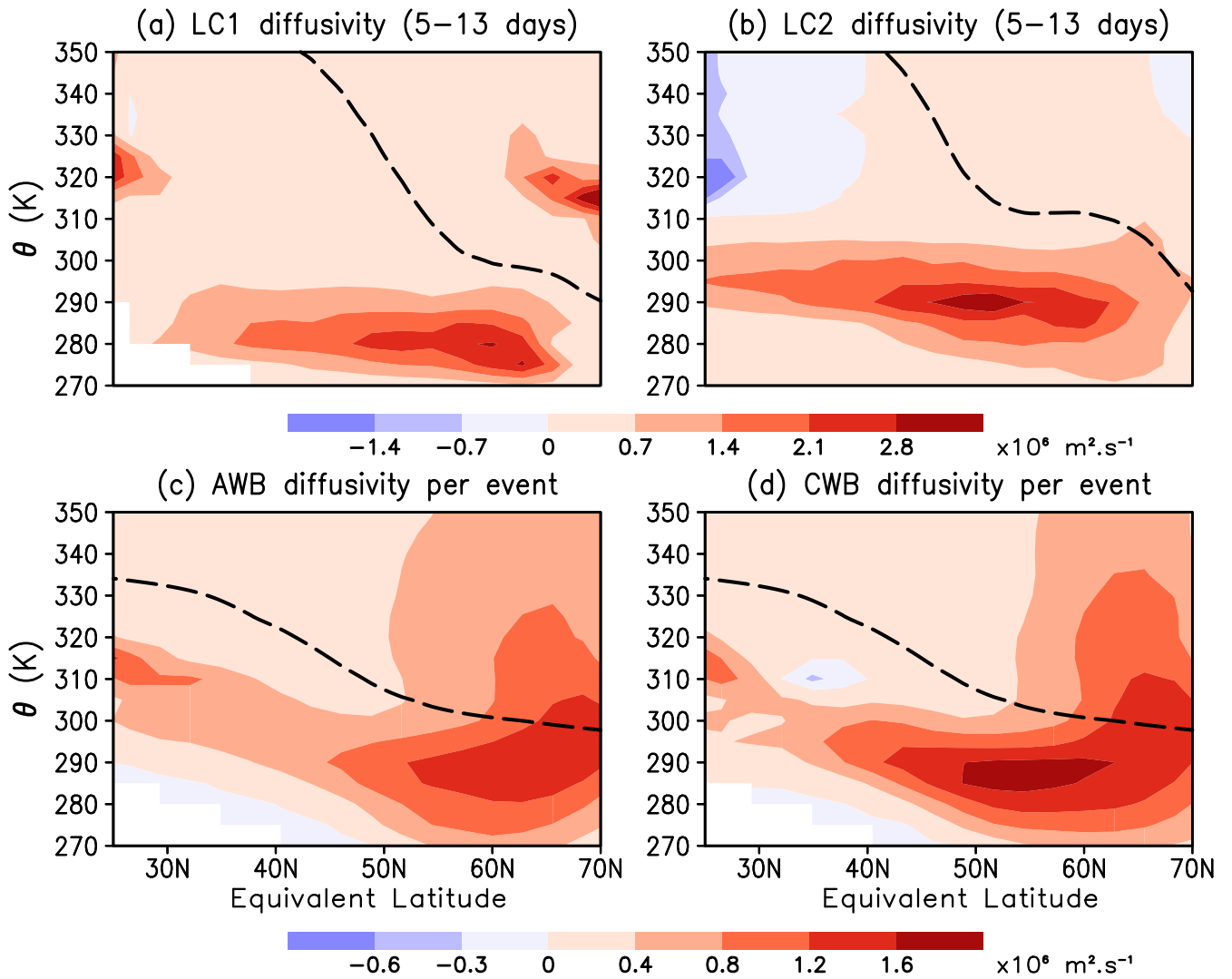


FIG. 7: **Upper row:** Eddy diffusivity (shading) as a function of approximate equivalent latitude in the idealized lifecycle simulations averaged over days 5-13 for (a) LC1, and (b) LC2. **Lower row:** Climatology of eddy diffusivity as a function of approximate equivalent latitude in the 25-year climate simulation for (c) anticyclonic wave breaking (AWB), and (d) cyclonic wave breaking (CWB), normalized by their respective frequency of occurrence.

## Underworld (270–295K)

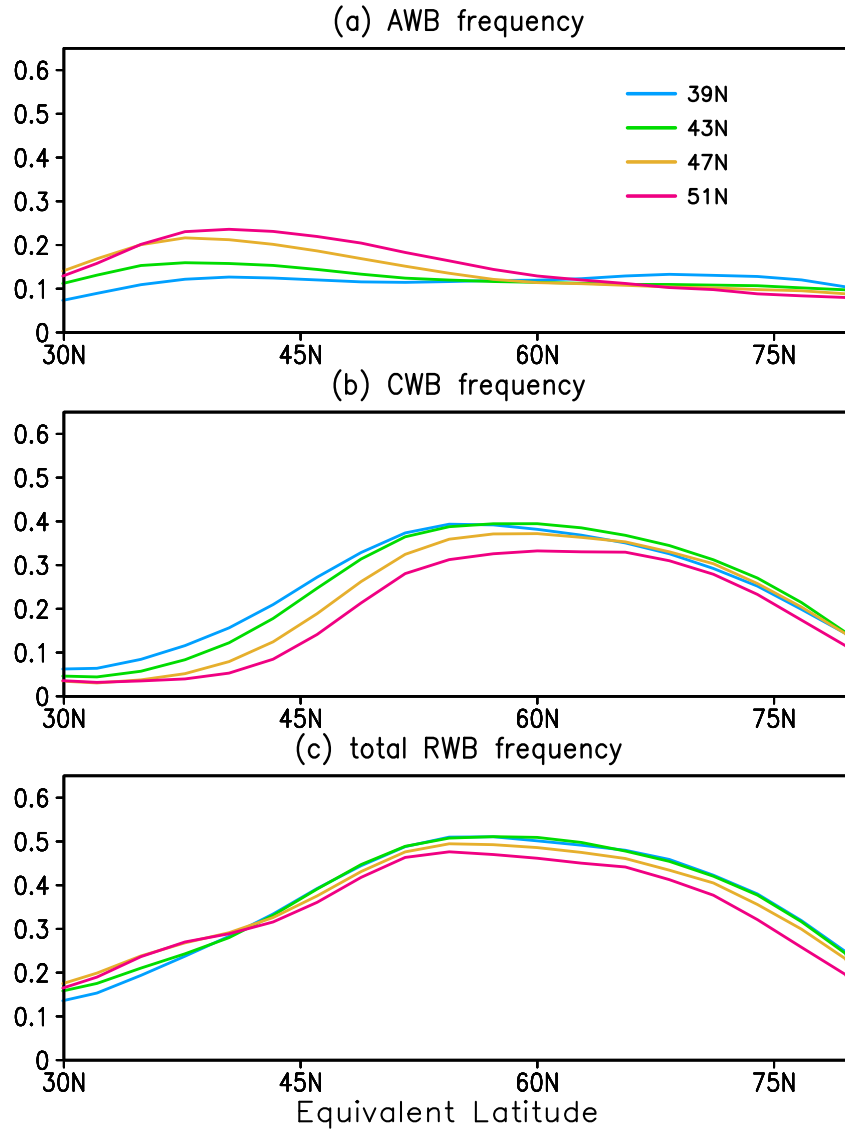


FIG. 8: Composite frequency of occurrence of Rossby wave breaking (RWB) as a function of approximate equivalent latitude with respect to various jet positions for (a) anticyclonic wave breaking (AWB), (b) cyclonic wave breaking (CWB), and (c) the total RWB in the underworld (270-295K).

## Underworld (270–295K)

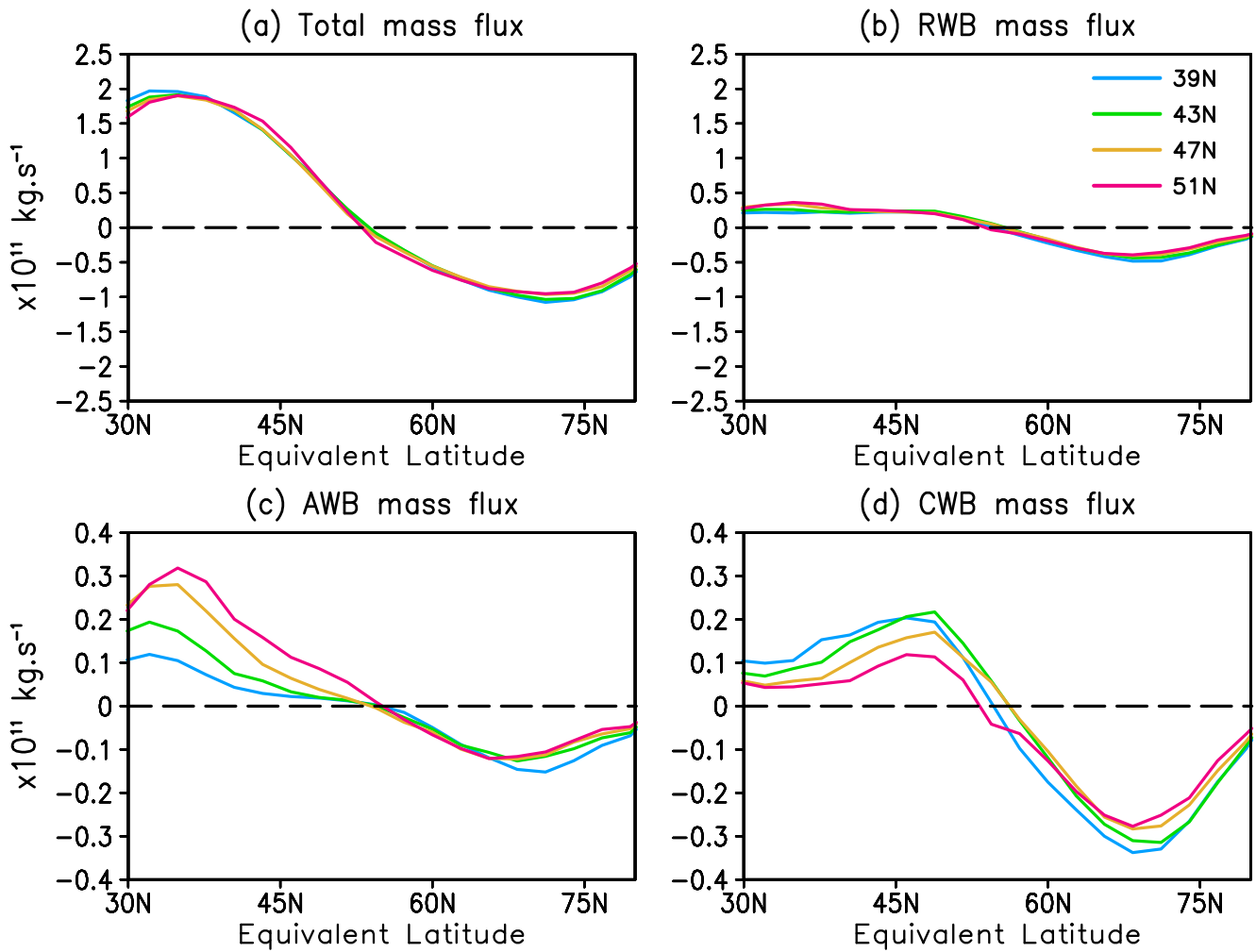


FIG. 9: Composite mass flux (unit:  $1 \times 10^{11} \text{ kg/s}$ ) as a function of approximate equivalent latitude in the underworld with respect to various jet positions for (a) the total, (b) Rossby wave breaking (RWB), (c) anticyclonic wave breaking (AWB), and (d) cyclonic wave breaking (CWB).

## Underworld (270–295K)

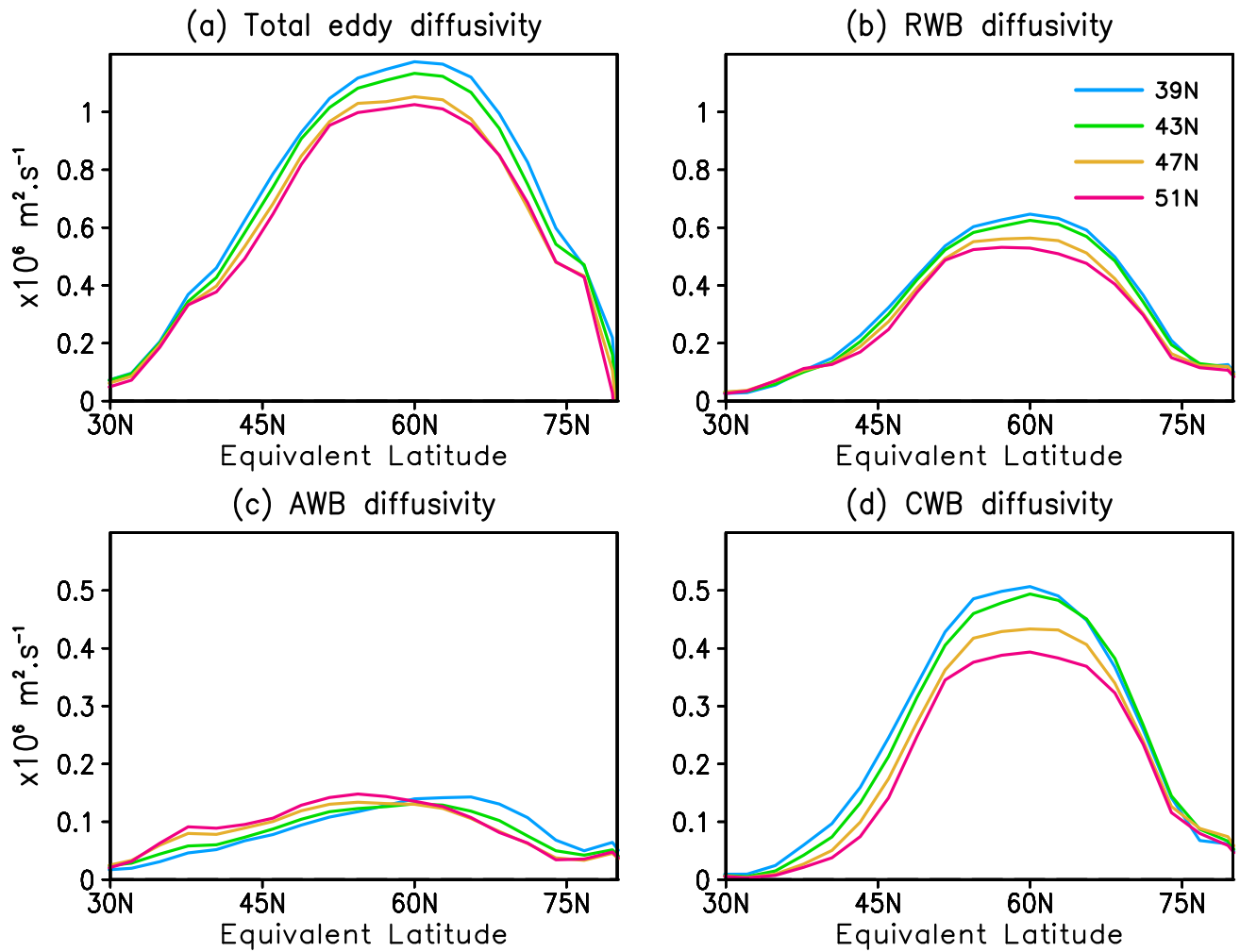


FIG. 10: Composite eddy diffusivity (unit:  $1 \times 10^6 \text{ m}^2 \text{ s}^{-1}$ ) as a function of approximate equivalent latitude in the underworld with respect to various jet positions for (a) the total, (b) Rossby wave breaking (RWB), (c) anticyclonic wave breaking (AWB), and (d) cyclonic wave breaking (CWB).

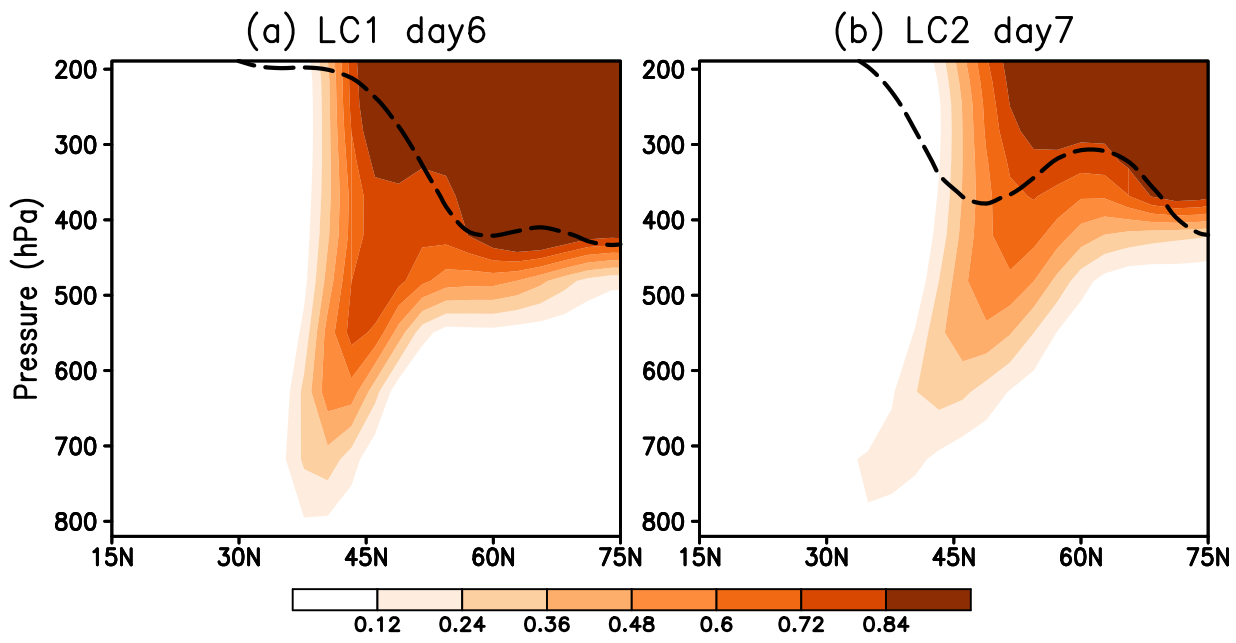


FIG. 11: Snapshots of stratospheric tracer concentration (shading) in the (a) LC1, and (b) LC2 idealized lifecycle simulations on the day of maximum intensity. The black dashed line denotes the zonal-mean contour of 2PVU averaged over the eddy life cycle.

## Middleworld (300–350K)

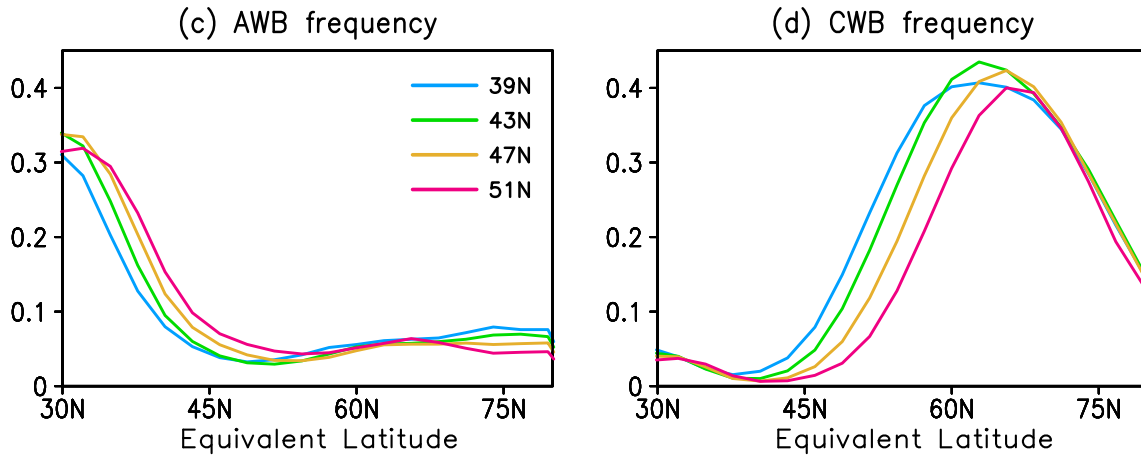


FIG. 12: Composite frequency of occurrence of Rossby wave breaking as a function of approximate equivalent latitude with respect to various jet positions for (a) anticyclonic wave breaking (AWB), and (b) cyclonic wave breaking (CWB) in the middleworld (300-350K).

## Stratosphere–Troposphere Exchange

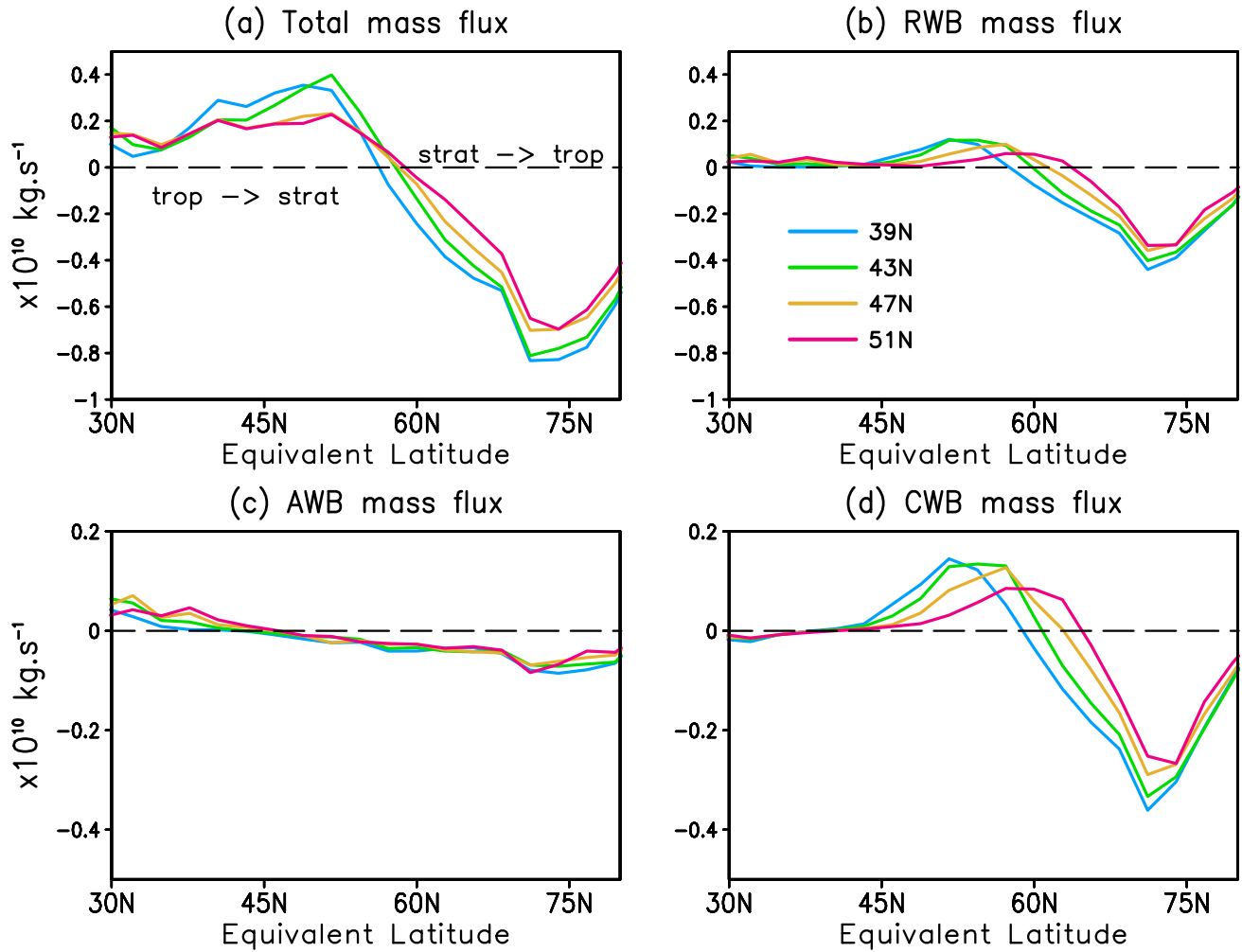


FIG. 13: Composite mass flux (unit:  $1 \times 10^{10} \text{ kg/s}$ ) across the dynamical tropopause due to asymmetric mixing with respect to various jet positions for (a) the total, (b) Rossby wave breaking (RWB), (c) anticyclonic wave breaking (AWB), and (d) cyclonic wave breaking (CWB).

## Stratosphere–Troposphere Exchange

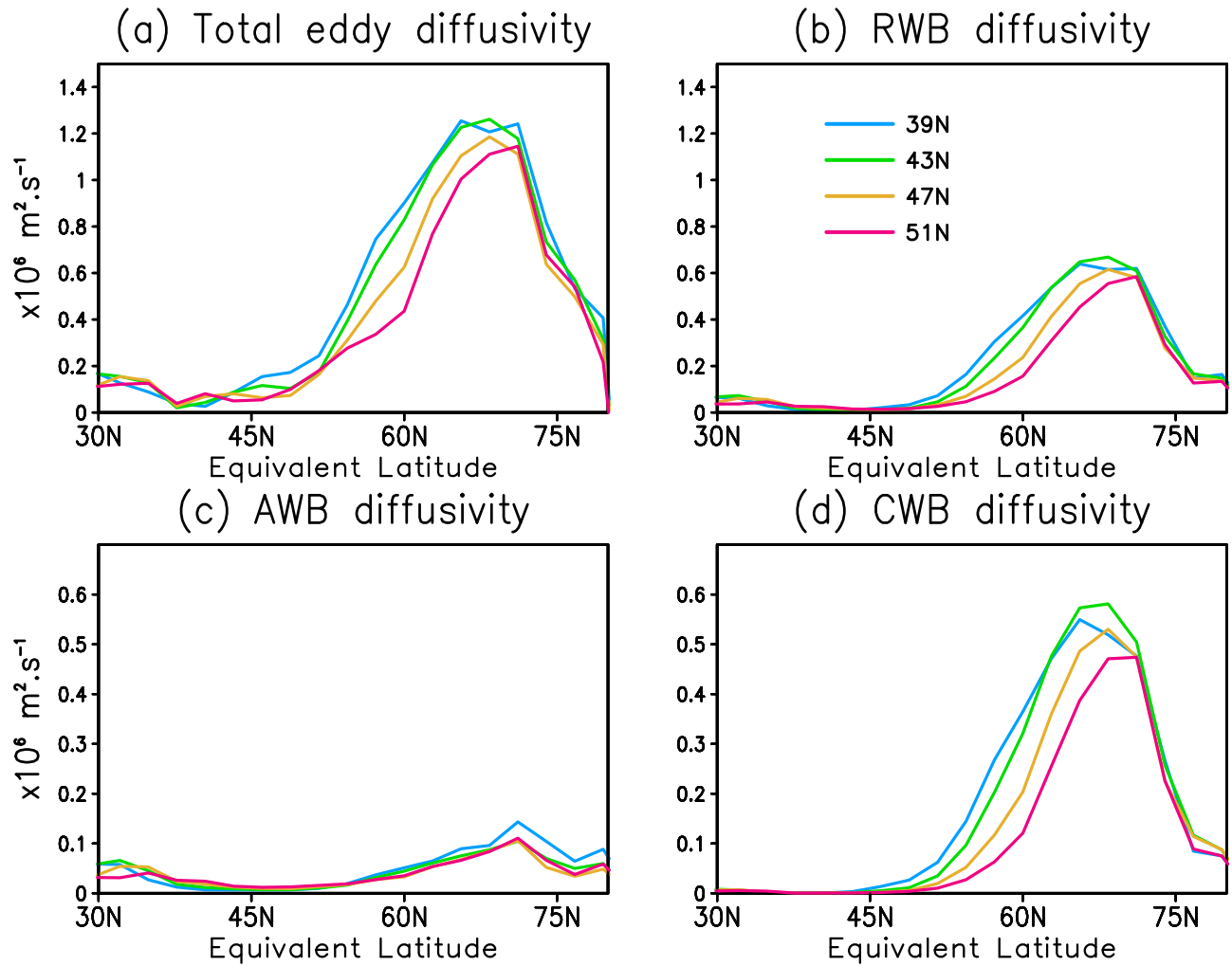


FIG. 14: Composite eddy diffusivity (unit:  $1 \times 10^6 \text{ m}^2 \text{ s}^{-1}$ ) as a function of approximate equivalent latitude along the dynamical tropopause with respect to various jet positions for (a) the total, (b) Rossby wave breaking (RWB), (c) anticyclonic wave breaking (AWB), and (d) cyclonic wave breaking (CWB).